Energy Conversion and Management, Volume 274, December 2022, Article number 116461
DOI: 10.1016/j.enconman.2022.116461

The novel Carbon Nanotube-assisted development of highly porous $CaZrO_3$-CaO xerogel with boosted sorption activity towards high-temperature cyclic CO_2 capture

Mohammad Heidari [a,b], *Seyed Borhan Mousavi* [c,d], *Farhad Rahmani* [b,1], *Peter T. Clough* [d], *Serap Ozmen* [d]

[a] Faculty of Chemical & Petroleum Engineering, University of Tabriz, Tabriz, Iran

[b] Department of Chemical Engineering, Faculty of Engineering, University of Kurdistan, Sanandaj, P.O.Box 66177-15175, Iran

[c] J. Mike Walker '66 Mechanical Engineering Department, Texas A&M University, College Station, TX, USA

[d] Energy and Power Theme, School of Water, Energy and Environment, Cranfield University, Bedford, Bedfordshire, MK43 0AL, UK

Abstracts:

Herein, for the first time, we employed three minor concentrations of Carbon Nanotubes (CNT), 2.5, 5, and 10 wt.%, as an auxiliary additive to boost the textural and structural features and CO_2 capture potential of sol-gel-derived Zr-supported CaO adsorbents. The corresponding xerogels were developed with 15/1 and 30/1 Ca/Zr molar ratios to minimize the required amount of prohibitive Zr-based precursor. For both types of Zr-decorated CaO adsorbents, 5 wt.% of CNT was recognized as the most efficient amount. In addition to 15.84 and 33.1% reduction in CaO crystallite sizes, 50.57 and 90.55% increments in pore volume values were reported for CaO adsorbents developed with 15/1 and 30/1 Ca/Zr molar ratios,

[1] Corresponding Author.
Email address: *F.rahmanichiyane@uok.ac.ir*

respectively. Over 15 cycles under harsh CO_2 capture conditions, the total amount of captured CO_2 for both abovementioned types of Zr-promoted adsorbents raised from 2.01 and 1.96 to 2.92 and 3.01 g CO_2/ g adsorbent, sequentially. Zr-promoted CaO nanoadsorbents merged with 5 wt.% MWCNT showed the ultimate CO_2 capture capacity of 0.164 and 0.149 g CO_2/ g adsorbent for xerogel prepared with 15/1 and 30/1 molar ratios of Ca/Zr, respectively. Even though the xerogel containing a Ca/Zr molar ratio of 15/1 showed the best sorption durability and ultimate capture capacity, MWCNT more significantly affects the CaO xerogel developed with a Ca/Zr molar ratio of 30/1. It can be deduced that the low content of multi-walled CNT notably contributes to developing highly efficient and fluffy-like Zr-promoted xerogels containing minor concentrations of Zr-based species.

Keywords: CO_2 capture, Calcium looping, Sol-gel derived CaO sorbent, CNT additive, Bio-additive

Highlights:

* Novel MWCNT-assisted development of highly porous and robust $CaZrO_3$-CaO xerogel

* Possibility of employing low content of Zr additive in the presence of MWCNT template

* Presenting best textural and adsorptive features for samples merged with 5 wt.% CNT

* >50% boost in porosity and more uniform dispersion of $CaZrO_3$ by adding 5 wt.% CNT

* >45% increase in the total capture capacity by adding 5 wt.% CNT over 15 cycles

1. Introduction:

The considerable pollution in our planet's environment, including water and atmosphere, endangers our society [1, 2]. The catastrophic climate breakdown rising from CO_2 emission exacerbates the atmospheric CO_2 concentration [3, 4]. According to the Paris Agreement, Negative Emission Technologies (NETs) have been considered to diminish CO_2 emissions [5]. As one of the NETs, the CO_2 capture technique has brought numerous improvements through disparate methods [6, 7]. Diminishing the CO_2 emission, mainly emitted by the flue gas released from fossil fuel combustion processes, through CO_2 capture processes has notably engrossed the attention of researchers and environmentalists in this decade as an ongoing challenge [8-10]. Comparing avenues of CO_2 capture from industrial units, including pre-combustion [11-13], oxy-combustion [14, 15], and post-combustion [16, 17], reveals the effectiveness of post-combustion methods, namely membrane [18], cryogenic [19], absorption [20], and adsorption [21]. One of the most emerging and developing techniques to separate CO_2 from post-combustion flue gases is a second-generation calcium looping (CaL) technique, derived from chemical looping combustion technology [22], based on reversible CaO carbonation/regeneration [23, 24]. In addition to CO_2 adsorption, CaL has already been exerted for the biomass and methane reforming process, H_2 production, and thermochemical energy storage [25-27]. Moreover, this process has been demonstrated as the most energy-efficient and affordable technology for industrial decarbonization, among other developing CO_2 capture processes. Practically at the CaL process, CaO particles are repeatedly circulated between inter-connected carbonator and calciner fluidized bed reactors based on specified participles as follows:

(1) CO_2 uptake at carbonator through exothermic partial carbonation reaction between CaO and CO_2, containing from post-combustion flue gas in a volume concentration of 10–15

vol.% CO_2, at temperatures between 600-700°C, optimum calculated temperature to have fastest carbonation rate [28].

(2) CaO regeneration through $CaCO_3$ decomposition based on Eq. 1. the $CaCO_3$ circulated from carbonator to calciner and fresh $CaCO_3$ entered through makeup flow, imported to compensate deactivated CaO particles after several cycles, are calcined a temperature beyond 800°C and under inevitably high CO_2 concentration, 70-100 vol.% CO_2, arising from either external ingination of fuel or pure-O_2 combustion to supply the required heat for calcination [29],

$$CaCO_{3(s)} \rightarrow CaO_{(s)} + CO_{2(g)} \quad (1)$$

(3) Feeding back the regenerated CaO in the calciner to the carbonator to commence a new cycle.

The high theoretical CO_2 uptake potential, remarkable adsorption capacity at temperatures above 500°C, swift carbonation/regeneration kinetics, and the wide accessibility of CaO sources, as the practical boons of the CaL process, dramatically attract the consideration of scientific researchers [28].

After passing several multiple cycles during the CaL process, the sintering of CaO particles impresses their CO_2 capture activity. CaO sintering leads to forming of a thick layer of $CaCO_3$ (~100 nm) on the CaO surface, the regular breakdown of the porous configuration, and a significant reduction in the volume of active CaO surface area needed for capturing CO_2 molecules from flue gas [29]. Emanated from the sintering phenomenon, the CO_2 capture capacity of CaO particles has drastically diminished with the rising cycle number during the CaL process. The high tendency of CaO for sintering could be attributed to its lower thermal durability during calcination at a temperature above 800 ℃, owing to its lower Tamman temperature (~ 500 ℃) compared to the CaL process temperature [28, 29]. To

potentially increase the overall efficiency of CaO particles in the CaL process, developing high-thermal-durable CaO sorbents is required.

Motivated by tackling this predominant hurdle, numerous research in this decade focused on improving the thermal-resistance property and adsorption activity of CaO sorbents under various CaL conditions through efficient techniques. Previously proved by researchers, the incorporation of thermal-durable additives into agglomerated nanoparticles contributes to decreasing the agglomeration rate dramatically [30-32]. One of the most promising materials to mitigate agglomeration and the sintering rate of CaO particles is metal oxides, which also improve the sorption performance of CaO-based sorbents [28]. The findings on metal-promoted composites indicate that enhanced efficiency through metal incorporation for boosting the processing activity of materials [33, 34]. The addition of metal-based additives causes the formation of nano-size metal-based species that locate between CaO grains and hinder their agglomeration during the high-temperature CaO regeneration, resulting in higher free surface area and pore volume compared to unmodified counterparts. This textural modification stemming from the presence of metal-based promoters enhances the CO_2 sorption capacity at each cycle and sorption durability during the CaL process. Among diverse studied metal-based additives, such as La_2O_3, MgO, TiO_2, MnO_2, Cr_2O_3, ZrO_2, Al_2O_3, CuO, Y_2O_3, CeO_2, SiO_2, Nd_2O_3, NaCl [35], ZrO_2-promoted CaO sorbents have exhibited more promising CO_2 capture activity because of the formation of $CaZrO_3$ as promoter in the CaO texture. Radfarnia et al. [36] demonstrated the greater effectiveness of formed $CaZrO_3$ on improving the CO_2 uptake performance of CaO sorbents, two kinds of Canadian limestone, under severe CaL conditions compared to developed $Ca_9Al_6O_{18}$, MgO. The CO_2 separation efficiency of CaO sorbents doped with ZrO_2, La_2O_3, MgO, and Al_2O_3 through the sol-gel combustion method indicated the superior activity of ZrO_2-stabilized sample, retaining 71.5% of its primary CO_2 uptake potential after 100 consecutive

carbonation/calcination cycles under severe conditions. Antzara et al. [37] investigated the sorption performance of Zr-modified CaO sorbent, with a $CaO/CaZrO_3$ weight ratio of 66 wt.%/34 wt.%, in a lab-scale fluidized bed reactor under the realistic calciner condition, 920°C, and 80 vol.% CO_2 concentration. The modified sorbent held 70% of its primary uptake capacity and indicated 5 times higher ultimate sorption capacity than natural limestone after 20 repetitive cycles. In another study, it has been revealed that incorporating CaO sorbent with ZrO_2 using a sol-gel synthesis manner resulted in 88.9% higher ultimate CO_2 uptake potential and 2 times higher sorption durability during 10 consecutive multiple cycles compared to unmodified CaO [38].

As an efficient and novel method to increase the CO_2 uptake potential of CaO adsorbents, employing flammable materials to boost the sorbent porosity of CaO particles attracted significant attention due to the influence of porosity on the capture efficiency of CaO sorbents. By intermixing biomass materials, ignitable at high-temperature calcination in the furnace, they place in the inner zones of CaO texture. With the biomass-merged CaO adsorbents being calcined in the furnace, the combustion of biomass particles forms numerous macro- and meso-pores, which facilitates the diffusion of CO_2 molecules into CaO structure and expedites CO_2 sorption capacity during the carbonation stage. Accomplished investigations on pellet-size CaO sorbents have demonstrated the positive role of biomass materials on the porosity of the CaO sorbents. The removal of these templates in CaO texture during the calcination stage of preparation leads to the forming of notable pores in CaO texture associated with considerably porous CaO structure and higher accessible CaO sites. Using the template-assistance hydrothermal preparation technique and glucose and urea as carbon-based templates, the total amount of captured CO_2 by CaO over 10 multiple carbonation-calcination cycles increased by ~164% [39]. Moreover, the conducted CO_2 capture analysis under harsh CaL conditions exhibited a 142% increment in ultimate CO_2

capture capacity at the 10^{th} cycle by hydrothermally templating MgO-promoted CaO adsorbent with xylose template [40]. In another research, hydrothermally employing the inverse opal (IO)-like carbon-nanospheres-templated preparation method on $Ca_3Al_2O_6$-stabilized CaO adsorbent resulted in more than 3 times higher CO_2 capture durability and capacity [41].

Among numerous carbon-based materials utilized as a carbon-based materials, Carbon Nanotube (CNT) is distinguished by its tubular structure, and considered as the most suitable additive that increase the chemical and physical process efficiency [42-46]. It can be predict that the utilization of tubular CNT as the template creates bigger hollow zones. Even though this additive has not been recognized as cost-effective material, recently published studies reveal the capability of fabricating CNT material from biomass-derived sources, such as Stillage residue [47], Chlorella [48], Chitosan [49], Potato peels [50], and Cotton fiber [51], through utilitarian procedures, namely pyrolysis [52], microwave plasma irradiation [53], chemical vapor deposition [54], and mechanochemical treatment [55]. The novel proposed scenarios to manufacture CNT from the abovementioned biomass facilitates the implementation of CNT-including process in industrial units.

It can be concluded that doping CaO with ZrO_2 plays an efficient role in improving the CO_2 uptake activity and reducing sintering during the CaL process. It is worth noting that even though the incorporation of CaO with ZrO_2 leads to the form of $CaZrO_3$, which enhances the sorption durability of CaO particles, the content of free CaO to capture CO_2 molecules of flue gas gradually decreased due to the $CaZrO_3$ formation through the reaction of CaO with ZrO_2. Zr-based precursors have been recognized as costly materials worldwide. On the one hand, reduced ZrO_2 content added to CaO sorbents resulted in less deactivation resistance and lower sorption capacity.

Considering the thorough conducted literature review on the adsorption activity of CaO-based CO_2 sorbents, most studies corroborated the superior CO_2 capture potential and stability revealed the Zr-promoted CaO adsorbents; in addition, most research activities revealed that the utilization of high content of Zr-derived additives diminishes the accessible CaO amount and raise the sorbent cost. Moreover, to the best of our knowledge, neither has the investigation been paid to boost the CO_2 capture capacity of CaO adsorbents modified with minor ZrO_2 nor the incorporation of biomass template into Zr-supported CaO has been studied. Therefore, in this research, for the first time, MWCNT, as an auxiliary carbon-based additive, was merged with Zr-modified CaO sorbents containing minor ZrO_2 concentrations to develop novel MWCNT-templated $CaZrO_3$-stabilized CaO nanoadsorbents through sol-gel combustion synthesis technique, and affecting parameters, namely Ca/Zr molar ratio and MWCNT concentration, were comprehensively scrutinized. In the present paper, CNT-templated Zr-stabilized CaO sorbents with various CNT amounts, including 2.5, 5, and 10 wt.%, and high Ca/Zr molar ratios of 15/1 and 30/1 were developed by the sol-gel method. These sorbents' morphological characterizations and CO_2 uptake potential under severe CaL process conditions were comprehensively investigated. It is worth stating that incorporating MWCNT into cost-effective Zr-stabilized CaO sorbents results in a striking improvement in CO_2 capture activity.

2. Experimental

2.1. Materials:

The nitrate salts of calcium, $Ca(NO_3)_2.4H_2O$ from *Merck*, and zirconium, $ZrO(NO_3)_2.H_2O$, from *Sigma Alderich*, as calcium and promoter precursors, respectively, as well as citric acid, $C_6H_8O_7.H_2O$ from *Sigma Alderich*, as combustion agent, were employed to synthesize Zr-modified CaO powders. MWCNT, from *VCN material Company*, was also used as a nano-

scale bio-based additive. The physical properties of nano-additive MWCNT are noted in **Table 1**.

Table 1. Characterizations of MWCNT

Morphology	Diameter (nm)	Length (µm)	Purity (%)	Specific surface area (m^2/g)	Density (g/cm^3)
Tube shape	10-20	~ 30	≥ 98	200	2.1

2.2. Preparation:

Firstly, to efface the impurities on the surface of CNT particles and improve their homogeneous dispersal in a water-based solution during the sorbents' preparation, they were prewashed with 4 M HCl. f. The sol-gel combustion synthesis approach was applied to prepare all samples using citric acid as a combustion agent. Firstly, the appropriate amount of calcium nitrate and citric acids, with a Ca/citric acid molar ratio of 9/5, were dissolved into deionized water under persistent heating and stirring. As soon as the solution temperature exceeds 70 °C, the required amounts of citric acid and zirconium nitrate are specified by the corresponding Ca/Zr molar ratio (15/1 or 30/1) and a Zr/citric acid molar ratio of 9/5, were added to the mixture. The final solution was stirred under the isolated condition by inserting the vessel lid. Then, the mixture was agitated at 100 °C for 3 h. Afterward, the determined amount of MWCNT was transferred to the solution and mixed for 1 h at ambient temperature. The sol was kept at room temperature for 24 h to form a uniform soaked gel. The wet gel was desiccated in an oven at 150 °C for 3 h, creating hollow structures. To eliminate residual organic components, the arid samples were calcined at 850 °C for 1.5 h under airflow with a heating rate of 10 °C/min.

Table 2: Specifications of synthesized CaO-based samples

Sample	Ca/Zr molar ratio	CNT additive (wt.%)	Elemental composition (At. %) from ICP test		Inert material (wt.%)		Textural and structural properties of fresh samples							BET surface area of used samples (m^2/g)
							Surface area (m^2/g)		Pore volume (mm^3/g)		Pore diameter (nm)		Average CaO crystallite size (nm)	
			Ca	Zr	CaO	$CaZrO_3$	BET	Langmuir	BET_{total}	BJH	BET_{mean}	BJH		
Pure CaO	-	-	48.25	0	100	-	11.65	12.7	57.3	57.53	19.68	1.64	27	2.54
Ca/Zr molar ratio of 15/1														
CaZr15-C0	15/1	-	34.37	2.29	81.5	18.5	12.9	12.72	83.24	72.19	25.81	1.21	26.5	3.23
CaZr15-C2.5	15/1	2.5	40.05	2.66	81.5	18.5	13.6	15.73	80.37	80.37	23.64	1.21	25.6	4.64
CaZr15-C5	15/1	5	42.67	2.85	81.5	18.5	17.83	19.4	116.6	108.7	26.16	1.64	22.3	6.48
CaZr15-C10	15/1	10	47.01	3.13	81.5	18.5	13.59	15.58	88.77	91.74	26.12	1.64	25.4	5.47
Ca/Zr molar ratio of 30/1														
CaZr30-C0	30/1	-	48.62	1.62	90	10	11.23	10.86	54.17	50.4	19.3	7.99	29.6	2.64
CaZr30-C2.5	30/1	2.5	44.83	1.49	90	10	13.4	14.84	57.12	56.88	17.05	7.99	27.8	3.09
CaZr30-C5	30/1	5	51.09	1.7	90	10	20.63	22.8	93.25	96.04	18.8	9.22	19.8	5.32
CaZr30-C10	30/1	10	54.22	1.81	90	10	16.75	18.6	85.38	84.94	20.38	1.21	24.7	5.58

2.3. Characterization:

Using BELSORP MINI II appliance, BET (Brunauer, Emmett, Teller) specific surface area and BJH (Barrett, Joyner, Halenda) pore size distribution of the synthesized samples were measured by N_2 physisorption at 77 K. The sorbents were degassed at 300 ℃ for 3 h in a vacuum before determination.

The X-ray diffraction (XRD) analysis patterns were acquired utilizing Siemens 5 D500 X-ray diffractometer (Cu Kα, λ= 0.15406 nm) to recognize the formed phases in samples. The peak intensity data of samples were assembled over the 2Theta range of 10-80°. To calculate the CaO crystallite size by XRD pattern, D_{avg}, Debye–Scherrer's equation [56-58] was used:

$$D_{avg} = \frac{0.9 \times \lambda}{\beta \times \text{Cos}\,\theta} \quad (2)$$

where λ, β, and θ correspond to the radiation wavelength, the whole breadth at half of the peak maximum (radians), and the peak angular position, respectively. A fitting correlation, β_0, of 0.108° was considered for the peak broadening due to the property of the diffractometer.

The structural morphology and textural porosity of fresh and used adsorbents before and after the CO_2 uptake process was examined by scanning electron microscopy (SEM) characterization on FEI Quanta 200 microscope apparatus, coupled with Oxford INCA sight X energy-dispersive X-ray analysis (EDX) applying on SAMX detector to determine elemental distribution.

To measure the quantitative content of metals, Ca and Zr, in ultimate samples, inductively coupled plasma optical emission spectroscopy (ICP-OES) characterization was performed through the Varian Vista-PRO CCD Simultaneous ICP-OES instrument.

2.4. CO_2 capture measurement:

The CO_2 uptake behavior and thermal durability of prepared samples were tested via TGA (thermogravimetric analysis), TA Instruments Discovery SDT 650 for successive 15 multiple carbonation/regeneration cycles under the severe CaL condition. The severe CaL condition for the post-combustion CO_2 capture process generally consists of the following:

- The short time resistance of CaO in carbonator owing to high inlet flue gas velocity and low content of CO_2 (10-15 wt.%).
- The calciner's high CO_2 concentration (more than 70% vol.) is caused by combusting inlet fuel to the calciner to provide a high required temperature for CaO regeneration.

To acquire valuable CO_2 capture data during the severe-condition CaL process, the CO_2 capture activity of prepared CaO-based sorbent in this work was assessed under harsh CaL conditions. 15 calcination and carbonation cycles were performed for the cyclic TGA testing, starting with a zeroth calcination step. The carbonation step was carried out at 650 °C for 10 minutes under 15% CO_2 balanced with N_2 and calcination at 950 °C for 10 minutes under 100% CO_2. The total flow rate for all the steps was 50 mL/min.

TGA results are assessed by CO_2 sorption capacity (C_n: gr of adsorbed CO_2/ gr of the whole sorbent) and CaO conversion (X_n). CO_2 sorption capacity is calculated based on a mass increase of the sample during the carbonation stage as follows [28]:

$$C_n = \frac{m_{f,n} - m_0}{m_0} \quad (3)$$

where C_n and $m_{f,n}$ are CO_2 sorption capacity and mass of carbonated sample at the n^{th} cycle, and m_0 is related to the mass of the fresh sample prior to 1^{st} cycle.

CaO conversion is the conversion ratio of available CaO grains to formed $CaCO_3$ through the physical reaction with CO_2 according to the following equation [59]:

$$X_n = \frac{C_n}{0.785 \times W_{CaO}} : [0.785 = \frac{M_{CO_2}\ (=44.01)}{M_{CaO}\ (=56.077)}] \quad (4)$$

which W_{CaO} is attributed to the weight fraction of free CaO available in the sorbent; M_{CO2} and M_{CaO} are the molar mass of CO_2 and CaO, respectively. Even though the mass of the whole sorbent (CaO + inert species) is considered for C_n calculation, X_n reveals the fraction of reacted CaO with CO_2 to the entire CaO [60]. Since a considerable amount of extant CaO remains unreacted during CO_2 during adsorption in the carbonator due to the sorbent agglomeration and sintering, the X_n value is below 100 %.

3. Result and discussion:

3.1. Characterization

Table 2 lists the textural specifications, elemental analysis, inert materials weight percentage (%), and CaO crystallite size of fresh and used adsorbents. It is worth noting that the fresh and used adsorbents are referred to as adsorbents before and after passing 15 multiple cycles under realistic conditions in this study, respectively. There are the nominal $CaZrO_3$ weight percentages of 81.5 and 90 wt.% for sorbents prepared with Ca/Zr molar ratios of 15/1 and 30/1, respectively. To concede the preliminary considered Ca/Zr molar ratios of 15/1 and 30/1 for synthesizing samples, Ca/Zr molar ratios calculated based on the ICP results are presented in **Fig. S1a**, indicating the maximum error of ≤ 0.34% with stoichiometric outcomes. Consequently, the Ca/Zr molar ratios derived from ICP analysis validate the initial molar ratios for all synthesized sorbents. Based on BET_{mean} and BJH pore diameter results, it can be deduced that all prepared samples possess macro- and meso- and micro-pores stemming from the combustion of embedded CNT and $CaZrO_3$ dispersal between CaO nanoparticles. **Fig. 1a** exhibits that Langmuir surface areas and CaO crystallite sizes are linearly and inversely proportional to the measured BET surface area of all synthesized samples with correlation coefficients R^2 of 0.96 and 0.89, sequentially.

Additionally, **Fig. S1b** shows the linear proportion between BET pore volumes and BJH pore volumes for all synthesized CaO-based xerogels, validated with a correlation coefficient R^2 of 0.945. Incorporating CNT into CaO particles of CaZr15-C0 and CaZr30-C0 underlines increases in structural and textural features, including BET surface area and BJH pore volume, and reduction in CaO crystallite sizes. For samples with a 15/1 molar ratio of Ca/Zr, the highest, most BJH pore volume of 108.7 mm^3/g, and the smallest CaO crystallite size of 22.3 nm are reported in the case of CaZr15-C5 followed by CaZr15-C10 (91.74 mm^3/g and 25.4 nm), CaZr15-C2.5 (80.37 mm^3/g and 25.6 nm), and CaZr15-C0 (72.19 mm^3/g and 26.5 nm). Considering the morphological values of this cluster of sorbents, their BET and Langmuir surface area are in the order of CaZr15-C5 with 17.83 and 19.4 m^2/g, CaZr15-C2.5 with 13.6 and 15.73 m^2/g, CaZr15-C10 with 13.59 and 15.58 m^2/g, and CaZr15-C0 with 12.9 and 12.73 m^2/g, respectively. Among synthesized xerogels with a 30/1 molar ratio of Ca/Zr, CaZr30-C5 shows the highest BJH pore volume and the lowest CaO crystallite size value of 19.8 nm. The reported surface area amounts indicate that CaZr30-C5 possessed the most BET and Langmuir surface areas of 20.63 and 22.8 m^2/g, respectively, followed by CaZr30-C10 with 16.75 and 18.6 m^2/g, CaZr30-C2.5 with 13.4 and 14.84 m^2/g, and CaZr30-C0 with 11.23 and 10.86 m^2/g, respectively. As it is explicit for both clusters, the addition of MWCNT until 5 wt.% contributed to enhancing the surface area of Zr-promoted CaO, even though more than 5 wt.% MWCNT adversely affects the accessible surface-resident CaO area.

To numerically evaluate the effectiveness of CNT on textural and structural properties of CaZr15-C0 and CaZr30-C0, variation rates (%) in BET and Langmuir surface area, BJH pore volume, and CaO crystallite sizes by incorporating 2.5, 5, and 10 wt.% of CNT into CaZr15-C0 and CaZr30-C0 sorbents are illustrated in **Fig. 1b** and **c**, respectively. There are remarkable improvements in principal textural characteristics. The integration of 5 wt.% CNT into CaZr15-C0 results in 38.21, 52.51, and 50.57% increment in BET, Langmuir

surface area, and BJH pore volume quantities, respectively, and also a 15.84 % reduction in CaO crystallite size. In addition to a 33.1% reduction in CaO crystallite size, by merging CaZr30-C0 with 5 wt.% of CNT, BJH pore volume quantities, BET, and Langmuir surface areas increase 90.55, 83.7, and 109.94%, respectively. Based on reported improvement rates, it can be concluded that the combustion of embedded CNT into CaZr15-C0 and CaZr30-C0 forms higher volumes of pores and affects the distribution of durable Zr-based species, which leads to dwindling the micro-size CaO agglomerates. However, the textural characteristics drop by increasing the number of merged CNT contents from 5 wt.% to 10 wt.%. It can be noted that this phenomenon probably arises from the heterogeneous dispersal of excess CNTs into CaO texture between CaO NPs during the synthesis due to a larger volume of CNT particles, resulting in the asymmetrical pore formation and heterogeneous scattering of $CaZrO_3$ grains between CaO grains. With the MWCNT being increased from 5 wt.% to 10 wt.%, their particles formed bigger aggregates during the preparation, not completely overcome by the stirring force, which adversely affects their embedding into CaO texture. Accordingly, the macropore volume decreased in sorbent prepared with 10 wt.% MWCNT compared to counterparts with 5 wt.% due to the non-uniform distribution of template particles in the inner zone of CaO configuration. Additionally, the heterogeneous scattering of $CaZrO_3$ aggravated the agglomeration of CaO particles, conducive to decreased surface area and CaO crystallite sizes.

As a result, 5 wt.% can be considered the more suitable and optimum amount of CNT compared to 10 wt.% to have the most porous CNT-templated Zr-modified adsorbent with the best textural features, and increasing the MWCNT contents aggravate sorbents' porosity.

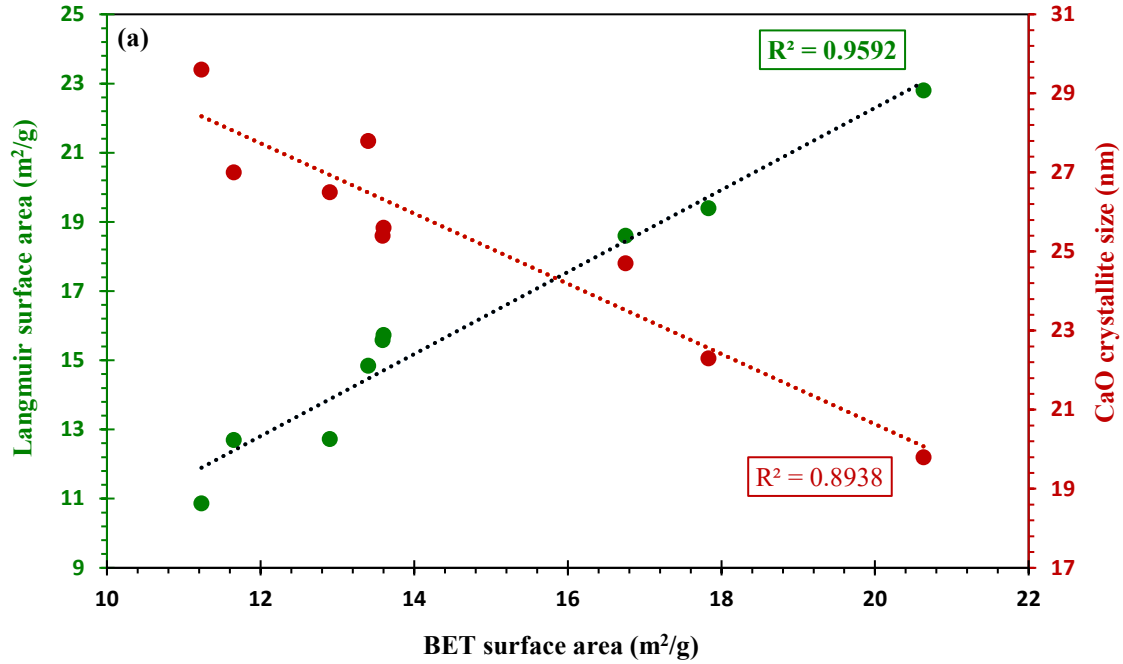
(a)
R² = 0.9592
R² = 0.8938
Langmuir surface area (m²/g)
CaO crystallite size (nm)
BET surface area (m²/g)
25
23
21
19
17
15
13
11
9
31
29
27
25
23
21
19
17
10
12
14
16
18
20
22

325

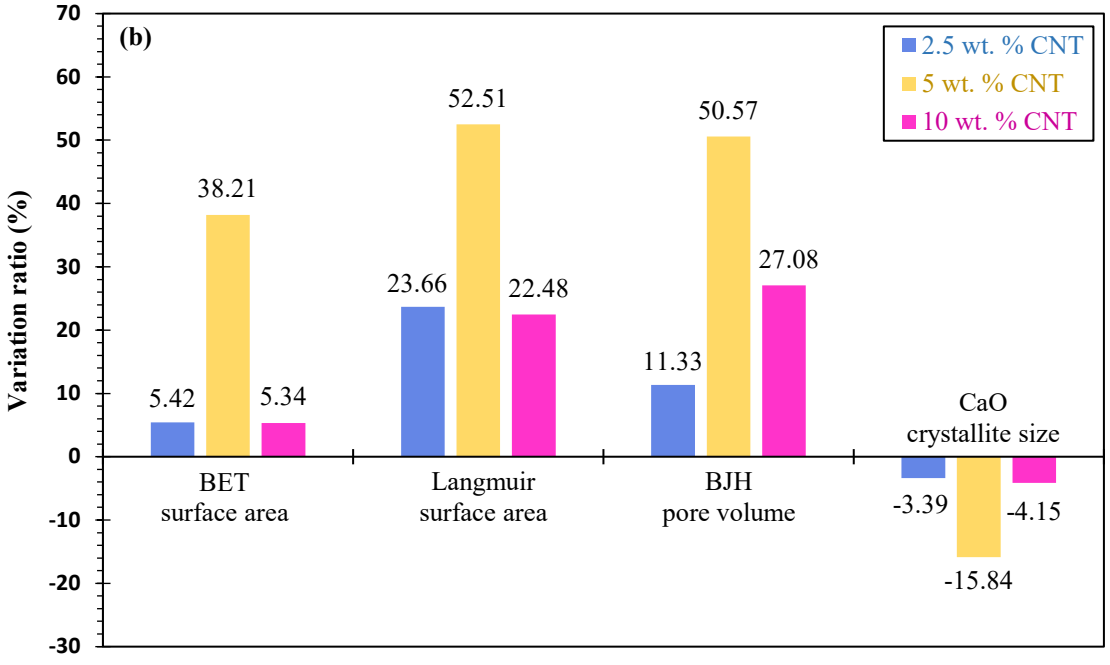
(b)
2.5 wt. % CNT
5 wt. % CNT
10 wt. % CNT
Variation ratio (%)
70
60
50
40
30
20
10
0
-10
-20
-30
5.42
38.21
5.34
23.66
52.51
22.48
11.33
50.57
27.08
-3.39
-15.84
-4.15
BET surface area
Langmuir surface area
BJH pore volume
CaO crystallite size

326

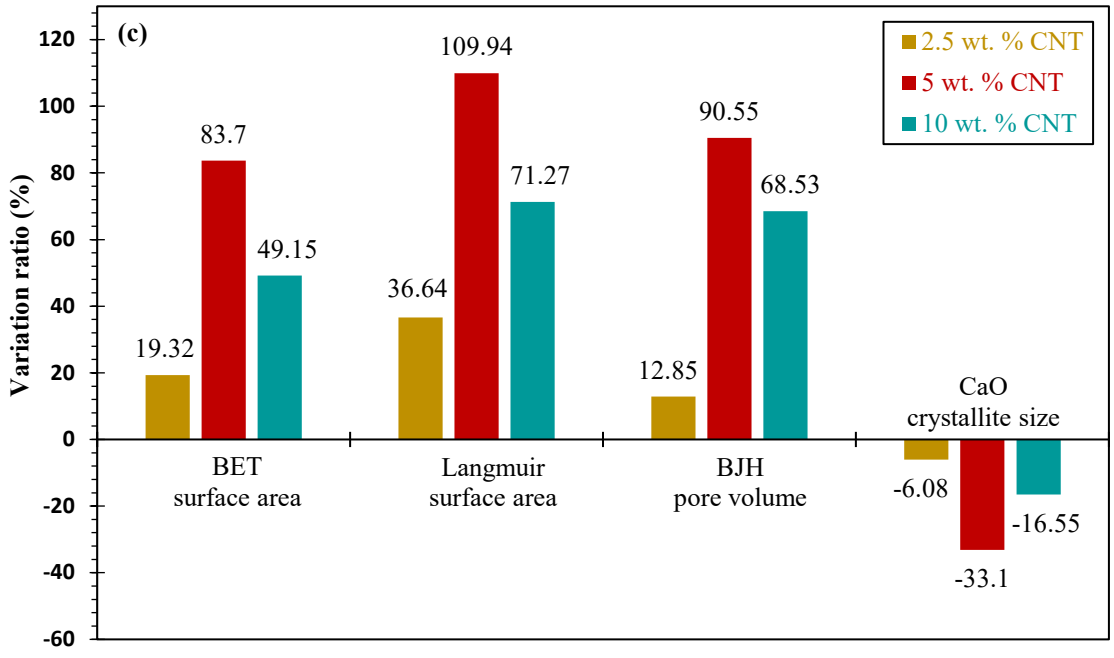

Fig. 1: (a) Langmuir surface area and CaO crystallite size of all developed Zr-decorated CaO-based xerogels versus BET surface area, and variation rate (%) of BET and Langmuir surface area, BJH pore volume, and CaO crystallite size by adding 2.5, 5, and 10 wt.% of CNT to (d) CaZr15-C0, and (e) CaZr30-C0.

The X-ray diffraction patterns of pure CaO, CNT-templated Zr-supported CaO adsorbent with Ca/Zr molar ratios of 15/1 and 30/1 over $10° \leq 2\theta \leq 80°$ are depicted in Figs. 2a and b. $CaCO_3$, $Ca(OH)_2$, and $CaZrO_3$ are the identified crystalline phases with high peak intensity. Since the sol-gel-derived synthesized CaO-based samples possess hygroscopic nature, the ambient moisture and CO_2 during the cooling step of calcination are adsorbed by CaO particles, resulting in the development of $Ca(OH)_2$ and $CaCO_3$ components identified in XRD characterization, due to Eqs. 6 and 7 [29]. According to Eq. 7, CO_2 gas molecules are also adsorbed by interfaces of formed $Ca(OH)_2$. $CaCO_3$ developed during post-calcination emerges in three diverse structures, β-$CaCO_3$, calcite, μ-$CaCO_3$, vaterite, and λ-$CaCO_3$, aragonite. The diversity in the type of developed $CaCO_3$ is related to the different CO_2 adsorption temperatures and the various adsorbers, including CaO and $Ca(OH)_2$. It is worth mentioning that the high-temperature pre-carbonation stage purges CaO particles from physisorbed CO_2 and/or H_2O molecules that facilitate CO_2 capture at the carbonation step.

The sol-gel combustion synthesis procedure readily develops a temperature of ≥ 1000 ℃. As Eq. 8 shows, by diffusing Ca^{2+} into the ZrO_2 lattice, $CaZrO_3$ species are produced via a solid-state reaction between CaO and ZrO_2, eased with the annealing phenomenon at the temperature above 1200 ℃ [28]. Comparing the XRD patterns reveals that CaZr15-C5 possesses $CaZrO_3$ peaks with lower intensity and wider broadening than CaZr15-C10 arising from the homogeneous distribution of $CaZrO_3$ crystallites between CaO particles.

$$CaO_{(s)}+H_2O_{(g)} \rightarrow Ca(OH)_{2(s)} \quad (5)$$

$$CaO_{(s)}+CO_{2(g)} \rightarrow CaCO_{3(s)} \quad (6)$$

$$Ca(OH)_{2(s)}+CO_{2(g)} \rightarrow CaCO_{3(s)} \quad (7)$$

$$CaO_{(s)}+ZrO_{2(s)} \rightarrow CaZrO_{3(s)} \quad (8)$$

There is considerable diversity between the XRD patterns of CaZr15-C5 and CaZr15-C10. As it is apparent, in the case of CaZr15-C5, the peaks related to CaO-based phases, namely CaO, $Ca(OH)_2$, and $CaCO_3$, possessed lower intensity and more broadening compared to CaZr15-C10, indicating its smaller CaO grain size presented in **Table 2**. These patterns corroborate that the additional MWCNT, more than 5 wt.%, adversely influences the porosity of CaO texture, resulting in a bigger CaO crystallite size due to the heterogeneous dispersal of 10 wt.% CNT particles into CaO texture during the preparation. It can be stated that this trend for sorbents containing 5 and 10 wt.% CNT is partially observed for samples prepared with a Ca/Zr molar ratio of 30/1. On the other hand, Comparing the XRD patterns of CaZr30-C2.5 and CaZr30-C5 indicates that CaZr30-C5 presented the CaO-presenting peaks with lower intensity and more transverse width than those of CaZr15-C2.5. This phenomenon demonstrates the higher porosity, smaller CaO crystallite size, and decreased CaO agglomerates growth in CaZr30-C5 compared to CaZr30-C2.5, corroborating the highly efficient content of 5 wt.% CNT for both kinds of Zr-promoted CaO adsorbents.

Fig. 3 exhibits N_2 adsorption/desorption isotherms for all synthesized samples. All adsorbents illustrate similar trends classified as reversible type II isotherms, which generally demonstrate a macro-porous texture and unlimited monolayer-multilayer adsorption up to high P/P_0 [61]. With an increase in the P/P_0, monolayer adsorption is completed, and the multilayer adsorption commences on the inner surface, an indicator of mesoporous structure [62, 63]. Derived by the capillary condensation of N_2 molecules into multilayers of mesoporous structure in the P/P_0 varied between the high pressure of 0.8-1, isotherms of CNT-templated sorbents possess the hysteresis loop type of H3, non-rigid aggregates of plate-like particles associated with slit-shaped pores. The abovementioned hysteresis type II isotherm consists of a network of meso and macropores, completely unfilled through pores' condensate. The higher amount of N_2 was adsorbed by CaZr15-C5 and CaZr30-C5 among prepared xerogels with 15/1 and 30/1 molar ratios of Ca/Zr, respectively. It can be concluded that both sorbents, CaZr15-C5 and CaZr30-C5, possess high multilayer adsorption, indicative of structures containing a higher volume of meso and macropores [64-67].

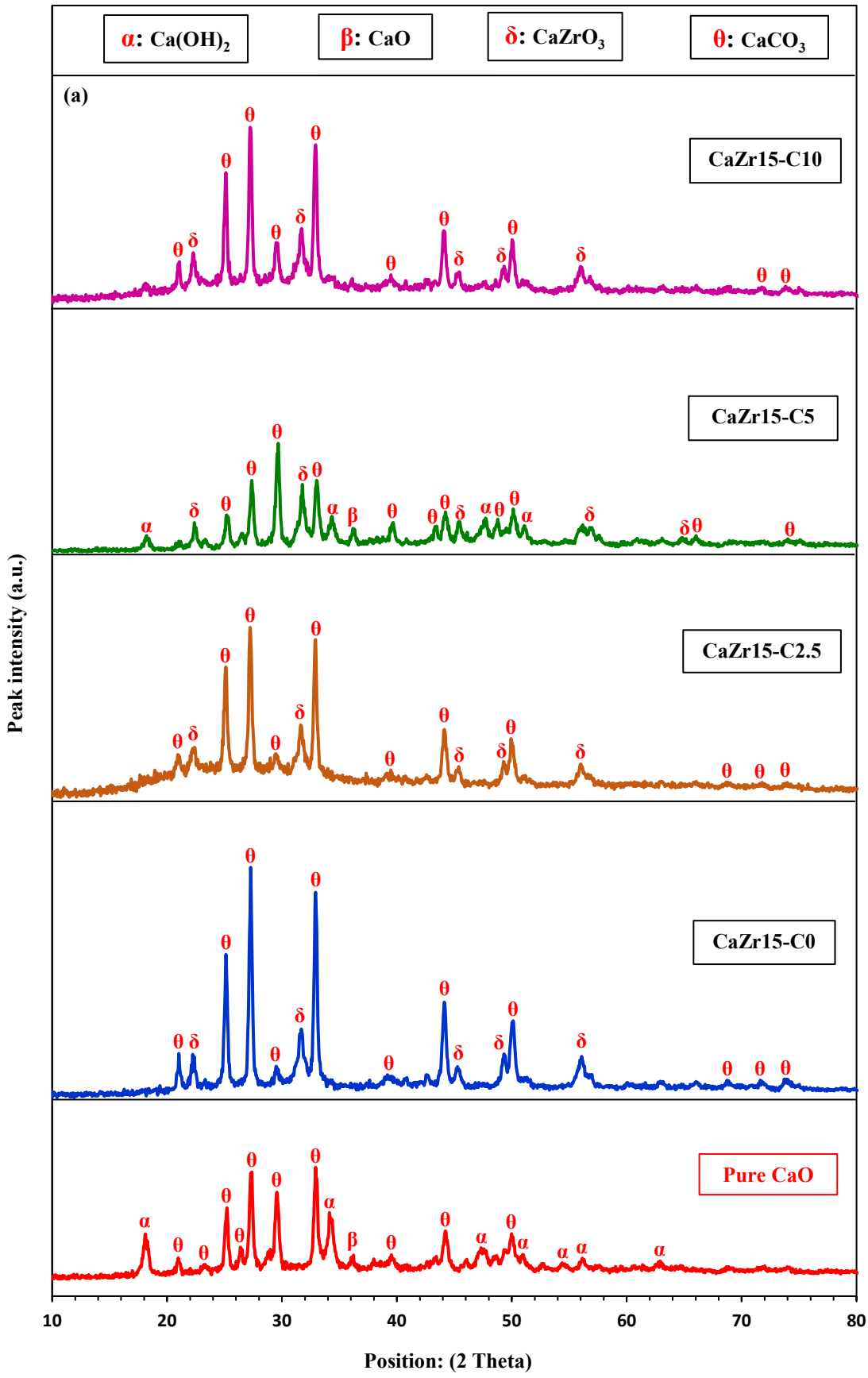
α: Ca(OH)2
β: CaO
δ: CaZrO3
θ: CaCO3
(a)
CaZr15-C10
CaZr15-C5
CaZr15-C2.5
CaZr15-C0
Pure CaO
Peak intensity (a.u.)
10
20
30
40
50
60
70
80
Position: (2 Theta)

380

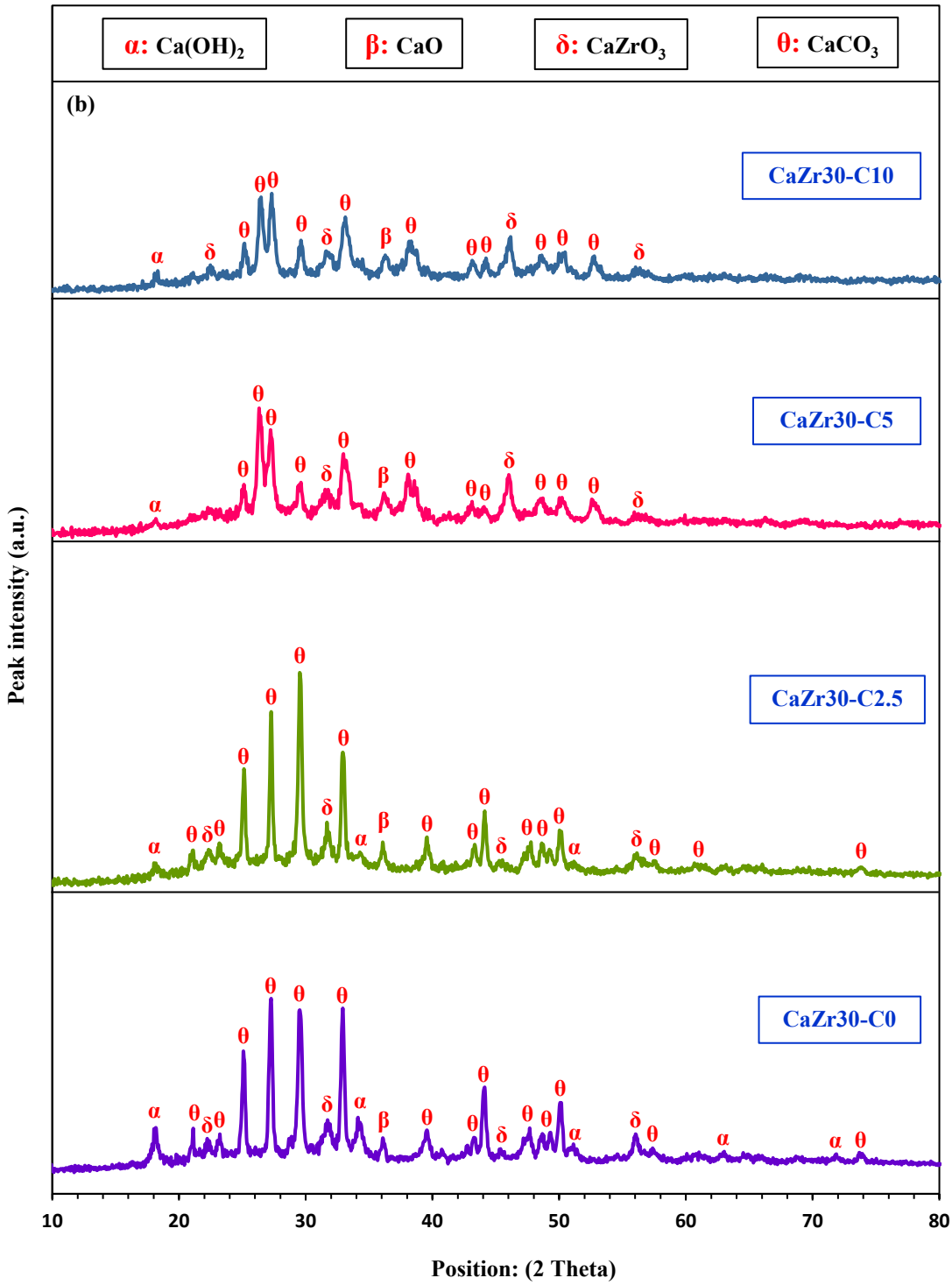

Fig. 2: XRD patterns of (a) pure CaO, CaZr15-C0, CaZr15-C2.5, CaZr15-C5, and CaZr15-C10, and (b) CaZr30-C0, CaZr30-C2.5, CaZr30-C5, and CaZr30-C10.

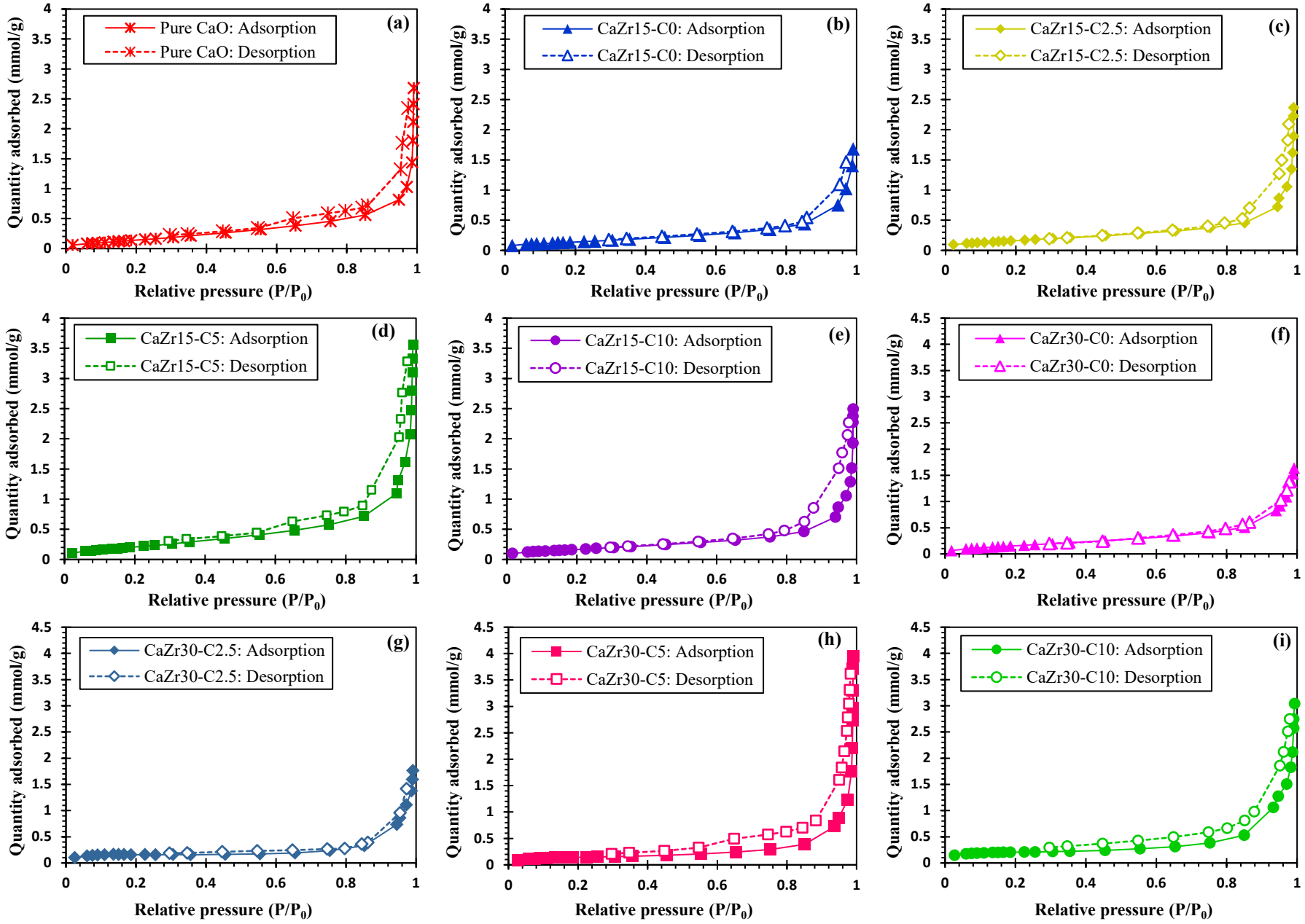

Fig. 3: N_2 adsorption/desorption isotherm of (a) pure CaO, (b) CaZr15-C0, (c) CaZr15-C2.5, (d) CaZr15-C5, (e) CaZr15-C10, (f) CaZr30-C0, (g) CaZr30-C2.5, (h) CaZr30-C5, and (i) CaZr30-C10.

BJH pore size distributions of pure CaO and both clusters of xerogels, prepared with 15/1 and 30/1 molar ratios of Ca/Zr, are presented in **Fig. 4a** and **b**. Even though pure CaO and prepared sorbents with Ca/Zr molar ratios of 15/1 mainly possess broad distribution of micropores, which have pores' diameters of 1-2 nm, the heterogeneous dispersal of pores is apparent for sorbents with a 30/1 molar ratio of Ca/Zr. As shown in **Fig. 4a**, **Fig. 1a**, and **Table 2**, the larger volume of micropores in the texture of CNT-templated samples indicates the effect of CNTs on increasing the pore volume into CaO configuration. Among exhibited BJH curves in **Fig. 4a**, CaZr15-C5 possesses a more significant amount of micropores, mesopores, and macropores. In addition to the effect of CNT removal on the formation of pores, the presence of an adequate amount of CNT during the sorbents' synthesis modify the dispersal of $CaZrO_3$; however, extra content of CNTs can underline the non-uniform scattering of CNTs and $CaZrO_3$ species into CaO structure, leading to a drastic reduction in pore volume and the formation of meso- and macro-pores. On the other hand, **Fig. 5b** demonstrates that incorporating 5 and 10 wt.% of CNT into CaZr30-C0 increases the volume of mesopores and micropores, respectively. A larger volume of macropores with a pore diameter of ≥80 nm is developed than CaZr30-C0. The significant differences in the type of formed pores in the cases of CaZr30-C5 and CaZr30-C10 can be attributed to the dispersal of CNTs into CaO structure during synthesis, which influences the distribution of formed $CaZrO_3$. It can be deduced that with the addition of the optimum amount of CNT, 5 wt.%, the formation of micro-, meso- and macro-pores enhanced, which shows its more porosity compared to CaZr15-C0 and CaZr30-C0. Among prepared xerogels with Ca/Zr molar ratios of 15/1 and 30/1, CaZr15-C5 and CaZr30-C5 possess the highest pore volume quantities.

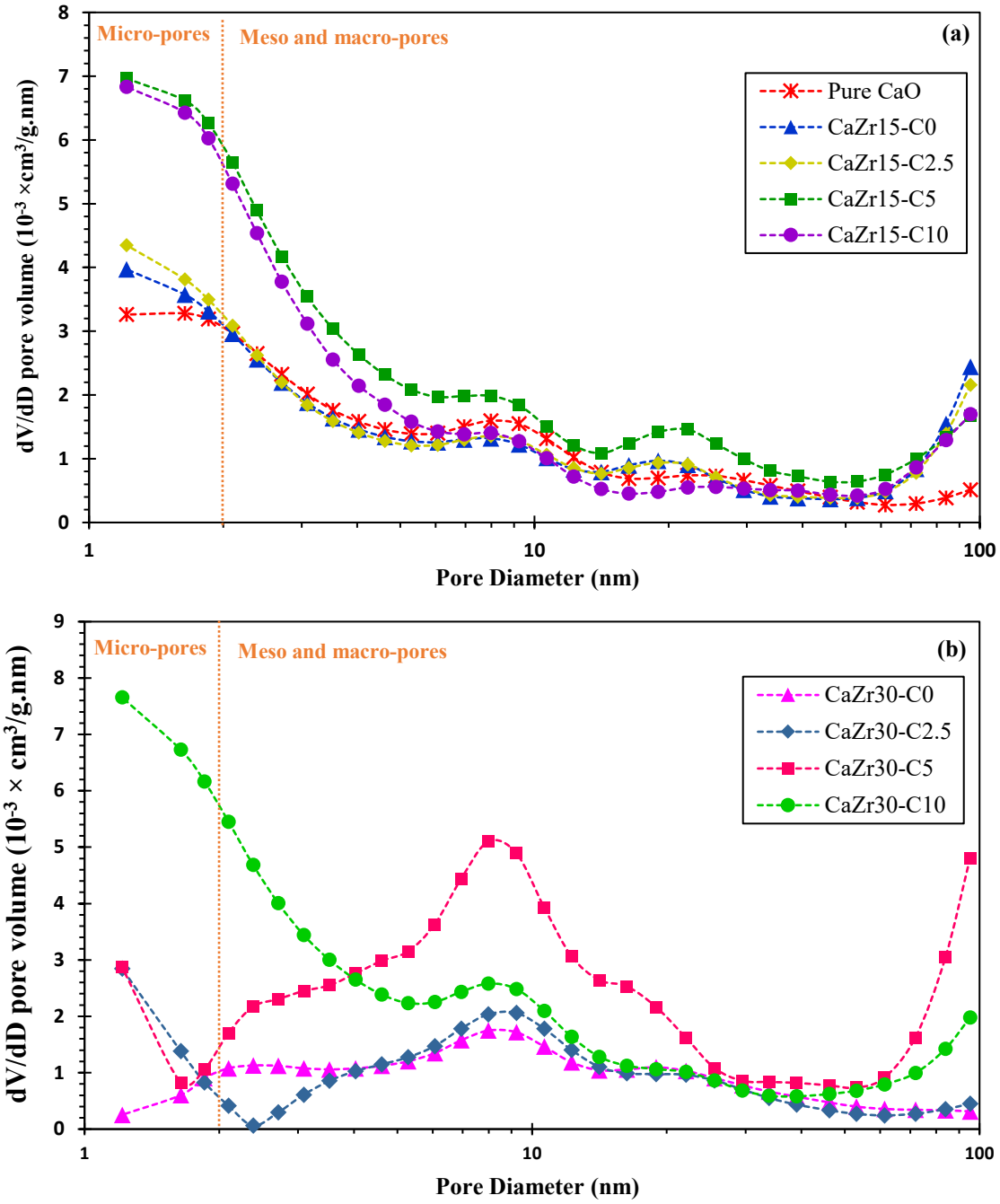

Fig. 4: Pore size distribution curves for (a) pure CaO, CaZr15-C0, CaZr15-C2.5, CaZr15-C5, and CaZr15-C10, and (b) CaZr30-C0, CaZr30-C2.5, CaZr30-C5, and CaZr30-C10.

FESEM images and EDX spectra of MWCNT and all developed samples with Ca-Zr molar ratios of 15/1 and 30/1 are illustrated in **Fig. 5** and **Fig. S2**. The EDX diagrams of Zr-promoted adsorbents in **Fig. S2** reveal the appearance of Zr, Ca, O, and C. The representative SEM pictures of MWCNT corroborate the tubular structure and its size and length nanometer scale. Pure CaO shows the clumpy structure and compact surface associated with the

residence of Ca, O, and C elements on the sorbent's surface. According to optical observation on SEM images of CaZr15-C0 and CaZr30-C0, the formation of $CaZrO_3$ moderately decreases CaO surface-present particle size and CaO micro-agglomerates. Comparing four prepared sorbents with a Ca/Zr molar ratio of 15/1, the porosity and the formation of fluffy zones are significantly improved by merging with CNT. The development of Zr-stabilized CaO adsorbents modified with 5 wt.% CNTs form the hollowest structure, associated with the smallest CaO surface-particles size. The most uniform scattering of $CaZrO_3$ among CaO particles in CaZr15-C5 is the main reason for its superior textural and morphological properties confirmed with BET-BJH and SEM illustrations. In the cases of prepared xerogels with a Ca/Zr molar ratio of 30/1, the efficient role of embedded CNT is manifest in presented SEM images. Identical to CaZr15-C0, with the addition of CNT, the CaO surface-resident grain size and agglomerates decrease, which underlies the emergence of fluffy areas. Among this cluster of sorbents, CaZr30-C5 presents more porosity. High conformity between reported textural and morphological characterizations in **Table 2** and depicted FESEM pictures can be observed. In addition to textural properties, namely BET surface area and BJH pore volume distribution, the morphology of CaZr15-C5 and CaZr30-C5 consist of more porous zones and smaller CaO surface-occupant sizes. Similarly, the representative FESEM pictures infer the efficient role of CNT in morphological properties of CaO particles and reducing the surface-resident CaO agglomerates.

Based on reported Ca/Zr mol.% of ~ 15 in **Fig. 1a**, the appearance of $CaZrO_3$ in the XRD patterns depicted in **Fig. 2**, and the elemental identification of Zr element via EDS spectra for developed Zr-modified adsorbents, it can be acclaimed that the employed synthesize method was suitable to develop the required adsorbents.

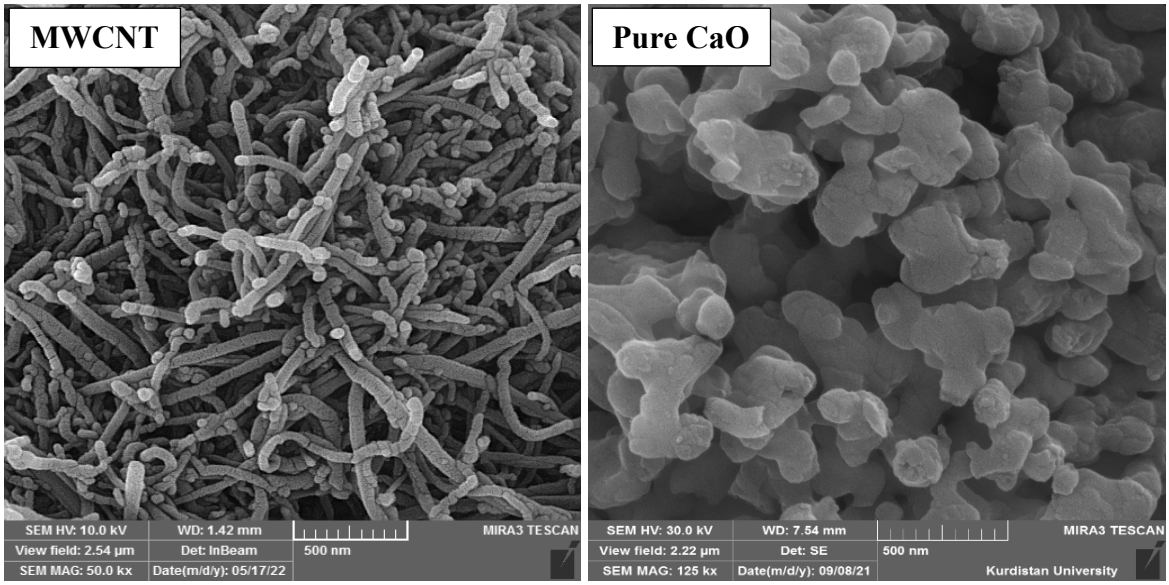
MWCNT
SEM HV: 10.0 kV
WD: 1.42 mm
MIRA3 TESCAN
View field: 2.54 µm
Det: InBeam
500 nm
SEM MAG: 50.0 kx
Date(m/d/y): 05/17/22
Pure CaO
SEM HV: 30.0 kV
WD: 7.54 mm
MIRA3 TESCAN
View field: 2.22 µm
Det: SE
500 nm
SEM MAG: 125 kx
Date(m/d/y): 09/08/21
Kurdistan University

445

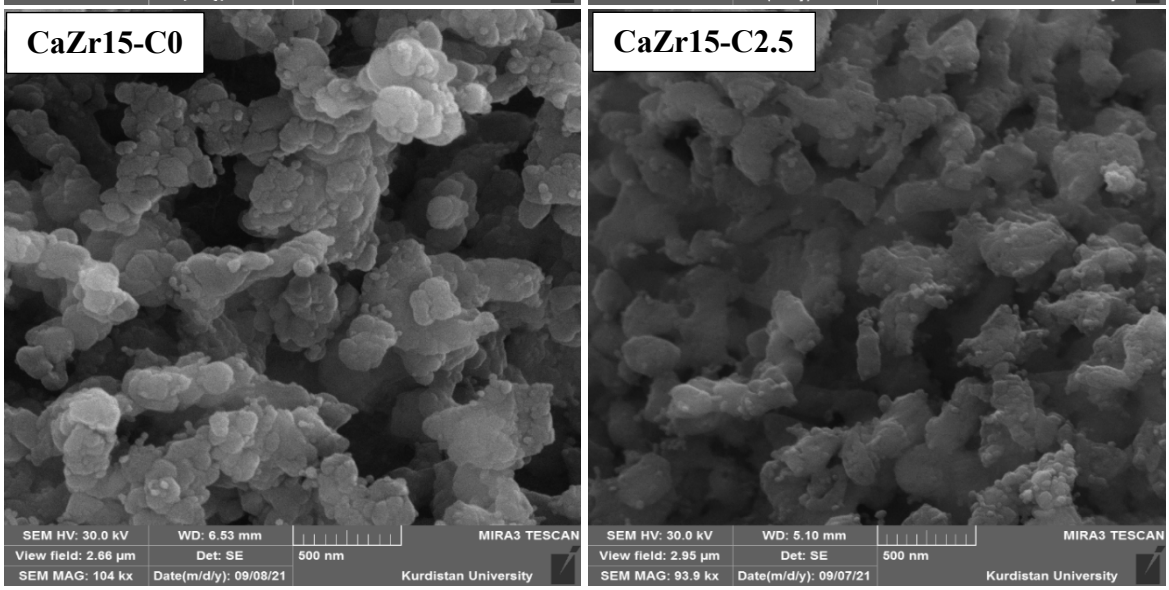
CaZr15-C0
SEM HV: 30.0 kV
WD: 6.53 mm
MIRA3 TESCAN
View field: 2.66 µm
Det: SE
500 nm
SEM MAG: 104 kx
Date(m/d/y): 09/08/21
Kurdistan University
CaZr15-C2.5
SEM HV: 30.0 kV
WD: 5.10 mm
MIRA3 TESCAN
View field: 2.95 µm
Det: SE
500 nm
SEM MAG: 93.9 kx
Date(m/d/y): 09/07/21
Kurdistan University

446

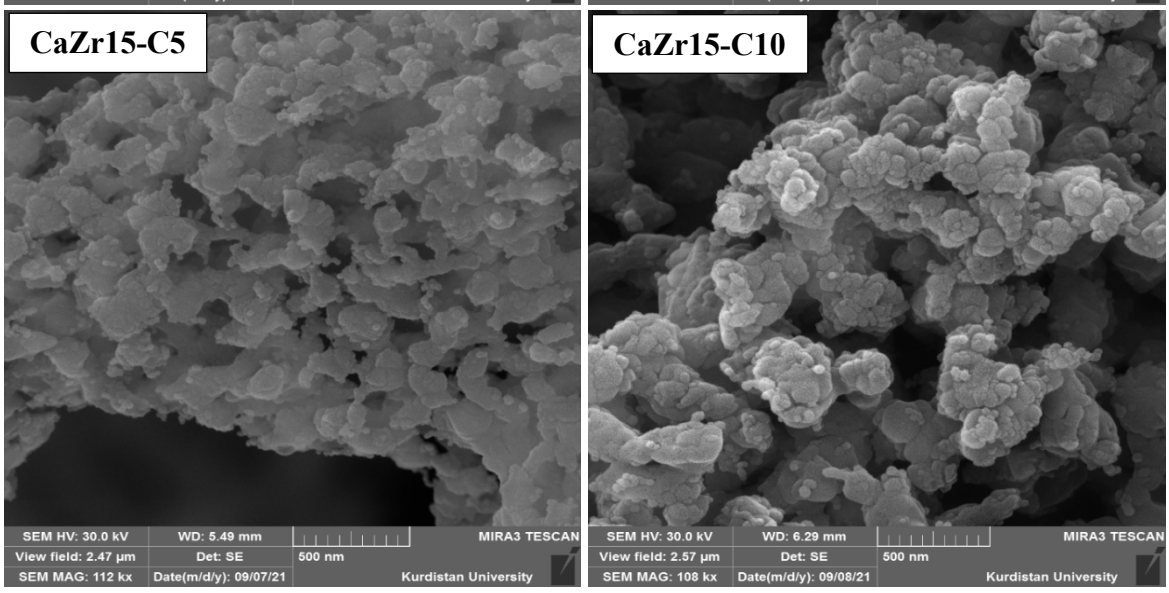
CaZr15-C5
SEM HV: 30.0 kV
WD: 5.49 mm
MIRA3 TESCAN
View field: 2.47 µm
Det: SE
500 nm
SEM MAG: 112 kx
Date(m/d/y): 09/07/21
Kurdistan University
CaZr15-C10
SEM HV: 30.0 kV
WD: 6.29 mm
MIRA3 TESCAN
View field: 2.57 µm
Det: SE
500 nm
SEM MAG: 108 kx
Date(m/d/y): 09/08/21
Kurdistan University

447

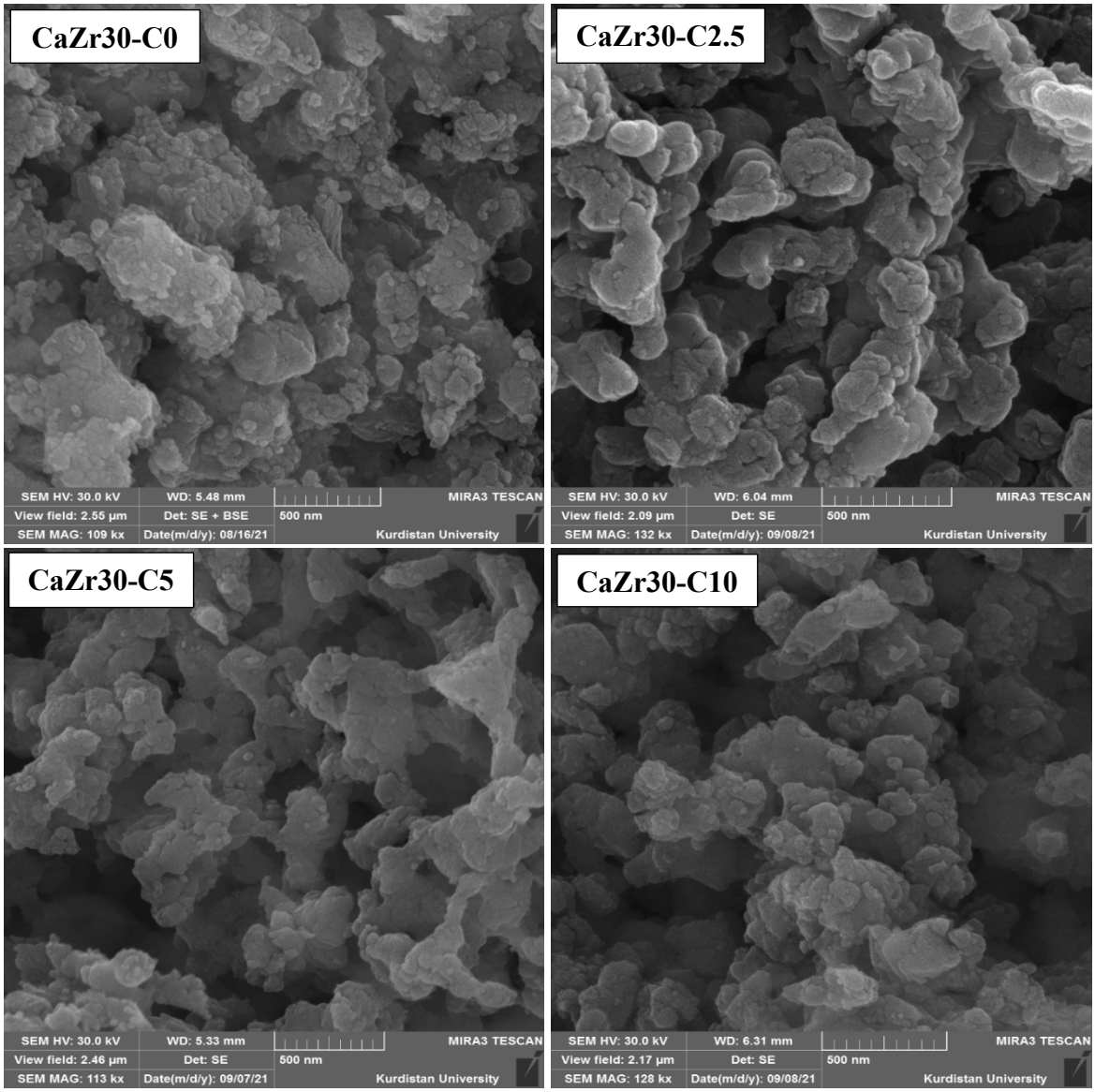

Fig. 5: SEM images of pure CaO, CaZr15-C0, CaZr15-C2.5, CaZr15-C5, CaZr15-C10, CaZr30-C0, CaZr30-C2.5, CaZr30-C5, and CaZr30-C0.

3.2. CO_2 capture activity

CO_2 capture activity of all synthesized sorbents to assess the influence of CNTs was analyzed under severe CaL conditions. CO_2 capture activity is evaluated by CO_2 capture capacity and CaO conversion curves versus the number of cycles.

The CO_2 uptake capacity and rate over carbonation time at 1st and 15 cycles for samples developed with Ca/Zr molar ratios of 15/1 and 30/1 are depicted in **Fig. S3** and **Fig. S4**, respectively, and discussions are included in **the supporting information file**. CO_2 adsorption capacity and CaO conversion values of untreated CaO and nano-scale xerogels

synthesized with Ca/Zr molar ratio of 15/1 over 15 multiple carbonation/calcination cycles under severe CaL conditions are depicted in **Fig. 6a** and **b**, respectively. Although the higher initial CO_2 capture capacity belongs to pure CaO, Zr-supported samples demonstrate superior CO_2 uptake capacity and CaO conversion. Improved with the homogeneous dispersion of $CaZrO_3$ and more formation of fluffy zones stemming from the combustion of embedded CNT, the CO_2 capture activity of CaZr15-C0 is enhanced in the presence of CNT. Furthermore, incorporating diverse contents of CNT into CaZr15-C0 significantly diminished the deactivation. Conformed with superior morphological and textural characteristics, CaZr15-C5 exhibits the highest CO_2 capture capacity and CaO conversion among CNT-templated samples. The CO_2 capture activity of all synthesized samples is listed in **Table 3**. The highest ultimate CO_2 capture capacity of 0.16 g CO_2/ g sorbent, most CaO conversion of 25.64 %, and the lowest uptake deactivation of 39.48 % belong to CaZr15-C5. Increasing the content of CNT from 5 to 10 wt.% aggregates cyclic activity due to the heterogeneous scattering of CNTs in the case of CaZr15-C10. Total amount of captured CO_2 during 15 multiple carbonation/calcination cycles is in order of CaZr15-C5 (2.92 g CO_2/ g sorbent) > CaZr15-C2.5 (2.62 g CO_2/ g sorbent) > CaZr15-C10 (2.56 g CO_2/ g sorbent) > CaZr15-C0 (2.01 g CO_2/ g sorbent). CaO conversion diagrams indicate the effectiveness of CNT on raising accessible CaO sites subjected to CO_2 molecules, in accordance with better morphological and textural properties of CNT-incorporated adsorbents. It is worth concluding that the 5 wt.% of CNT additive is the optimal amount for Zr-modified CaO sorbents.

CO_2 capture capacity values and calculated the CaO conversion amounts of untreated CaO, CaZr30-C0, CaZr30-C2.5, CaZr30-C5, and CaZr30-C10 over 15 CaL cycles under harsh conditions are plotted in **Fig. 6c** and **d**, sequentially. The CNT-merged samples demonstrate higher CO_2 uptake capacity and CaO conversion compared to CaZr30-C0, and

the superior performance belongs to CaZr30-C5, so a higher amount of CO_2 is captured by CaZr30-C5 in most cycles. Even though the analogous activity is presented by CaZr30-C5 and CaZr30-C10, due to less amount of employed CNT in CaZr30-C5, 5 wt.% CNT can be considered the optimum content to improve the cyclic activity of CaZr30-C0. The precise total amounts of captured CO_2 are in the order of CaZr30-C5 (3.01 g CO_2/g sorbent) > CaZr30-C10 (2.99 g CO_2/g sorbent) > CaZr30-C2.5 (2.13 g CO_2/g sorbent) > CaZr30-C0 (1.96 g CO_2/g sorbent).

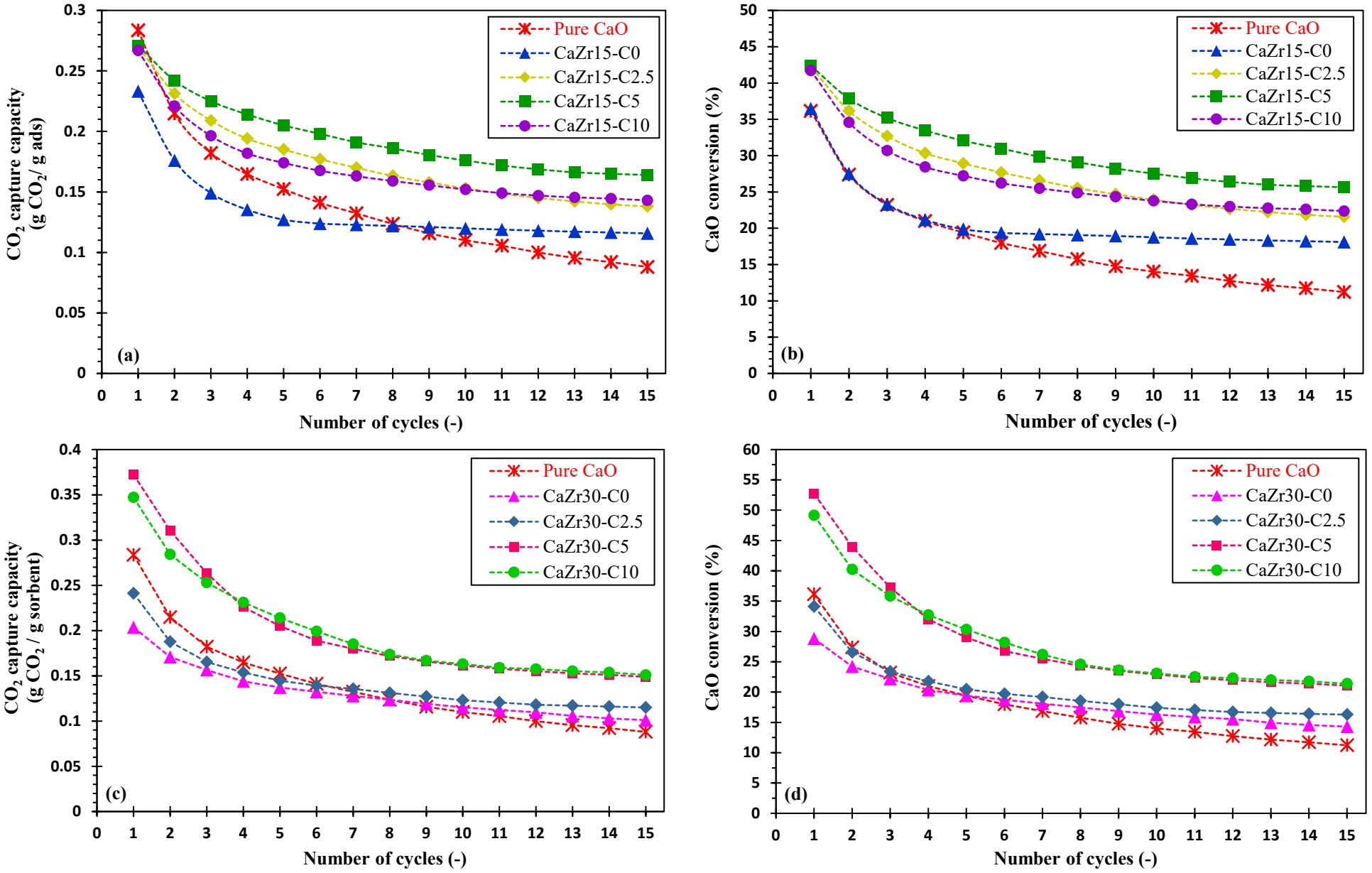

Fig. 6: CO_2 capture capacity and CaO conversion of samples developed with Ca/Zr molar ratios of (a and b, respectively) 15/1, and (c and d, respectively) 30/1, under severe CaL conditions

Table 3: Comparison of the CO_2 uptake activity of all developed sorbents

Sorbent	CO_2 capture capacity (g CO_2/ g sorbent)		CaO conversion (%)		The total amount of captured CO_2 (g CO_2/g sorbent) over 15 multiple cycles	Deactivation (%)
	1st cycle	15th cycle	1st cycle	15th cycle		
Pure CaO	0.2835	0.088	36.13	11.21	2.1	31.04
Ca/Zr molar ratio of 15/1						
CaZr15-C0	0.2332	0.1157	36.46	18.1	2.01	50.37
CaZr15-C2.5	0.27	0.138	42.22	21.58	2.62	48.88
CaZr15-C5	0.271	0.164	42.37	25.64	2.92	39.48
CaZr15-C10	0.2667	0.143	41.7	22.36	2.56	46.38
Ca/Zr molar ratio of 30/1						
CaZr30-C0	0.2035	0.101	28.81	14.3	1.96	50.38
CaZr30-C2.5	0.241	0.115	34.12	16.28	2.13	52.28
CaZr30-C5	0.372	0.149	52.71	21.07	3.01	60.02
CaZr30-C10	0.347	0.151	49.14	21.38	2.99	56.48

EDX dot-mappings of Ca and Zr elements occupied on the surface of CaZr15-C5 and CaZr15-C10 are illustrated in **Fig. 7**, which corroborates the more homogeneous dispersal of $CaZrO_3$ between CaO particles for CaZr15-C5. However, CaZr5-C10 possesses the clumpy scattering of Zr in some zones during the sorbent preparation. Despite the efficient role of CNT in increasing the fluffy areas and porosity, excessive addition of CNT, more than 5 wt.%, underlies the substantial decrease in CO_2 capture capacity and deterioration of the textural and structural characteristics, namely pore volume distribution and value, surface area, and CaO crystallite size. There is a highly remarkable correlation between EDX dot-mapping analyses and XRD patterns of CaZr15-C5 and CaZr15-C10. The CaZr15-C5 that

shows the $CaZrO_3$ peaks with slightly lower intensity and wider broadening has a more homogeneous $CaZrO_3$ dispersal than CaZr15-C10.

In order to investigate the morphological changes in CaZr15-C5 and CaZr15-C10 occurring during 15 multiple carbonation/calcination cycles under severe conditions, SEM pictures of used abovementioned samples are presented in **Fig. 8**, apparently revealing the sintering phenomenon in several areas. By comparing the SEM micrographs of fresh and used CaZr15-C5 and CaZr15-C10, larger CaO grains and CaO micro-agglomerates emanate after 15 multiple cycles leading to the significant reduction in free and accessible CaO particles for CO_2 adsorption and the limitation for the CO_2 diffusion into inner areas. The aforementioned mishaps are the central grounds for the sorption deactivation over the CaL process. There is a striking conformity between SEM micrographs and the ultimate CO_2 capture capacity of CaZr15-C5 and CaZr15-C10, in which used CaZr15-C5 captured a higher amount of CO_2 at the 15^{th} cycle possesses the lower sintered areas and more porous structure compared to used CaZr15-C10.

BET surface area of the used CaZr15-C0, CaZr15-C2.5, CaZr15-C5, and CaZr15-C10 are reported in **Table 2**. This enhancement in ultimate surface area value is acquired with the addition of MWCNT. The surface area values of 12.9, 13.6, 17.83, and 13.59 m^2/g, recorded for fresh CaZr15-C0, CaZr15-C2.5, CaZr15-C5, and CaZr15-C10, reduced to 3.23, 4.64, 6.48, and 5.47 m^2/g, stemming from the CaO agglomeration during the CaL process. Following the SEM images and ultimate sorption capacity (at the 15^{th} cycle), used CaZr15-C5 that presented better porosity and higher ultimate sorption capacity has more BET surface area of 6.48 m^2/g among developed samples with a Ca/Zr molar ratio of 15/1. As a result, the SEM images and BET surface area values corroborate the superior sorption performance of CaZr15-C5 compared to CaZr15-C0, CaZr15-C2.5, and CaZr15-C10.

Fig. 7 also shows the EDX dot. mapping of Ca and Zr for fresh CaZr30-C5 and CaZr30-C10. The widely distributed Zr element, related to the scattering of $CaZrO_3$ species between Ca, is visible. It should ne boted that the dispersion of inert phases considerably affects the materials' porosity, thermal durability and agglomeration [68-70]. These diagrams confirm the more uniform dispersal of CaO and $CaZrO_3$ for CaZr30-C5 and CaZr30-C10, apparently indicative of morphological improvement using CNTs. There are no significant differences in Zr scattering between CaZr30-C5 and CaZr30-C10. Based on visual morphological observations, 5 wt.% of CNT is sufficient to homogenize the $CaZrO_3$ dispersion among CaO grains.

FESEM pictures of used CaZr30-C5 and CaZr30-C10 over 15 multiple CaL cycles under severe conditions are presented in **Fig. 8**. The formation of sintered CaO cites, enlarging CaO grain size. The aggregation of surface-located CaO particles is evident in the sorption deactivation of CaZr30-C5 and CaZr30-C10 over multiple CaL cycles because of developing sintering-favored $CaCO_3$ layers during the process. Comparing the depicted SEM images of fresh CaZr30-C5 and CaZr30-C10 with used counterparts demonstrates that fluffy-like zones, the volume of pores, and accessible CaO particles gradually decline over the multicycle process.

Reported BET surface area values for used MWCNT-incorporated sorbents with the Ca/Zr molar ratio of 30/1 in **Table 2** indicates the significant decrement in surface area values after passing 15 multiple CaL cycles under harsh condition. These surface area values verified the calculated ultimate sorption capacity for CaZr30-C0, CaZr30-C2.5, CaZr30-C5, and CaZr30-C10; CaZr30-C10 with the highest capture capacity at 15^{th} cycles, 0.151 g CO_2/ g sorbent, possess the most surface area of 5.58 m^2/g.

Fresh CaZr15-C5

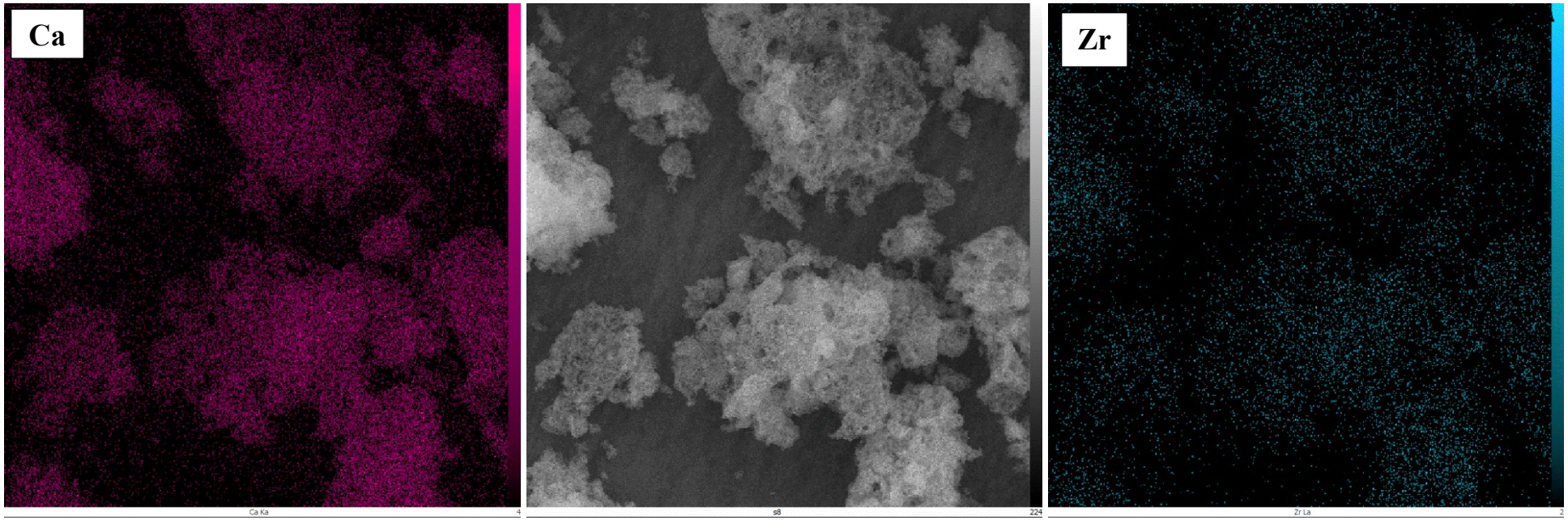

Fresh CaZr15-C10

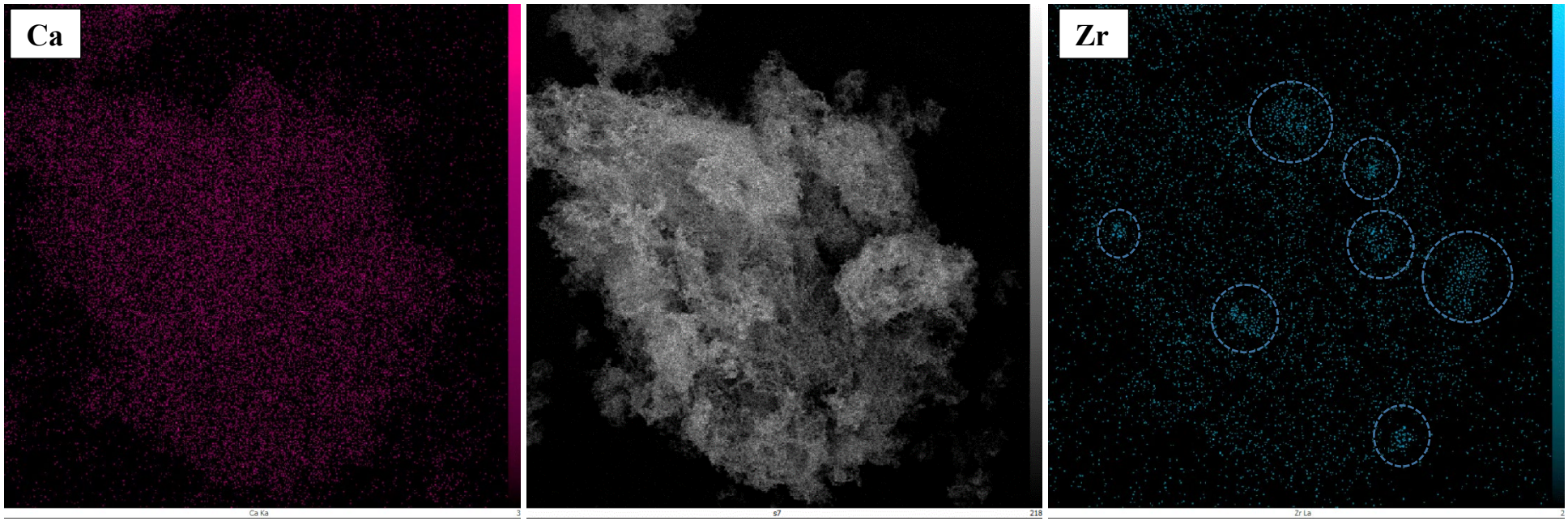

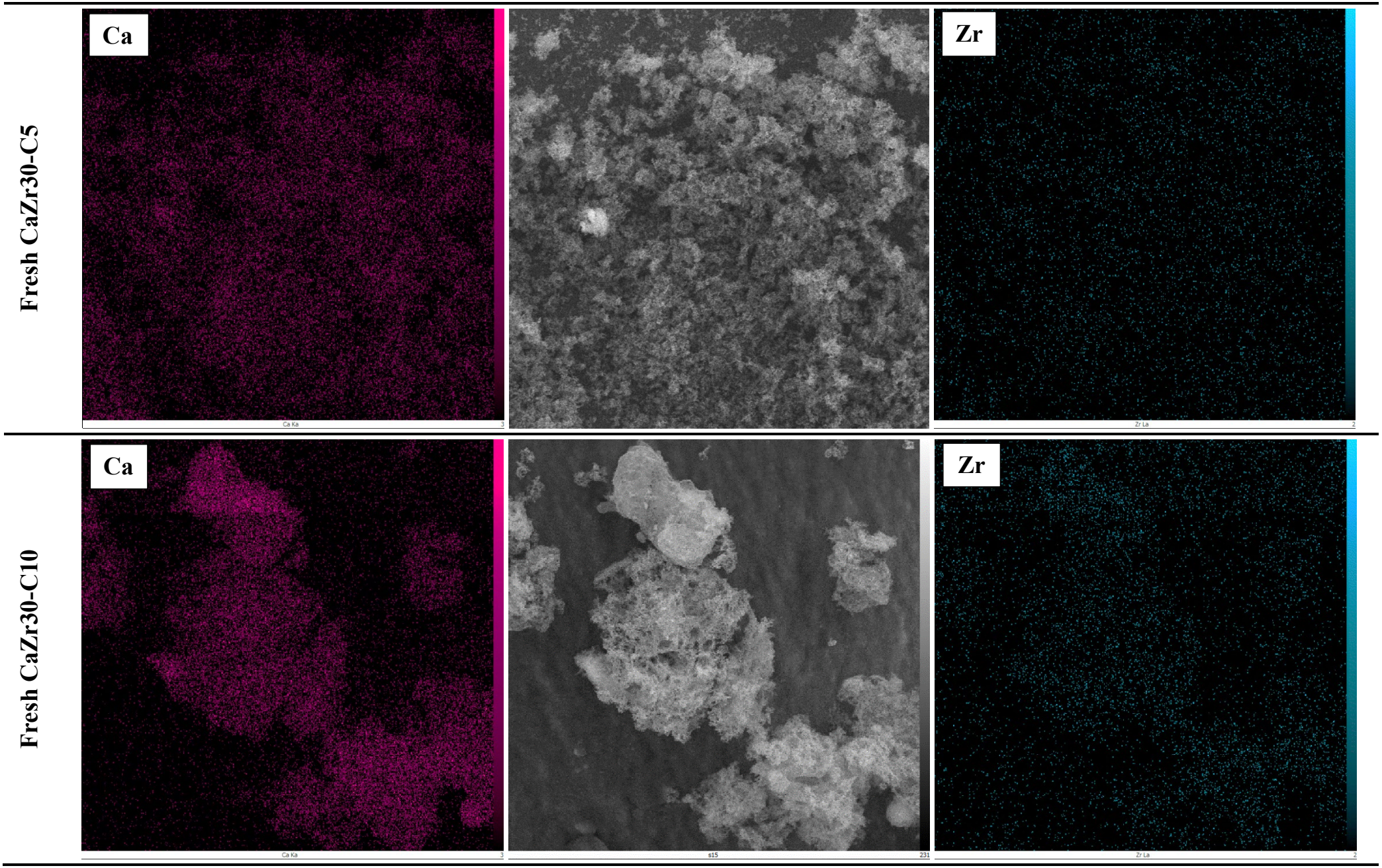

Fig. 7: EDX dot-mapping analysis of the distributed Ca and Zr elements into the textures of fresh CaZr15-C5, CaZr15-C10, CaZr30-C5, and CaZr30-C10

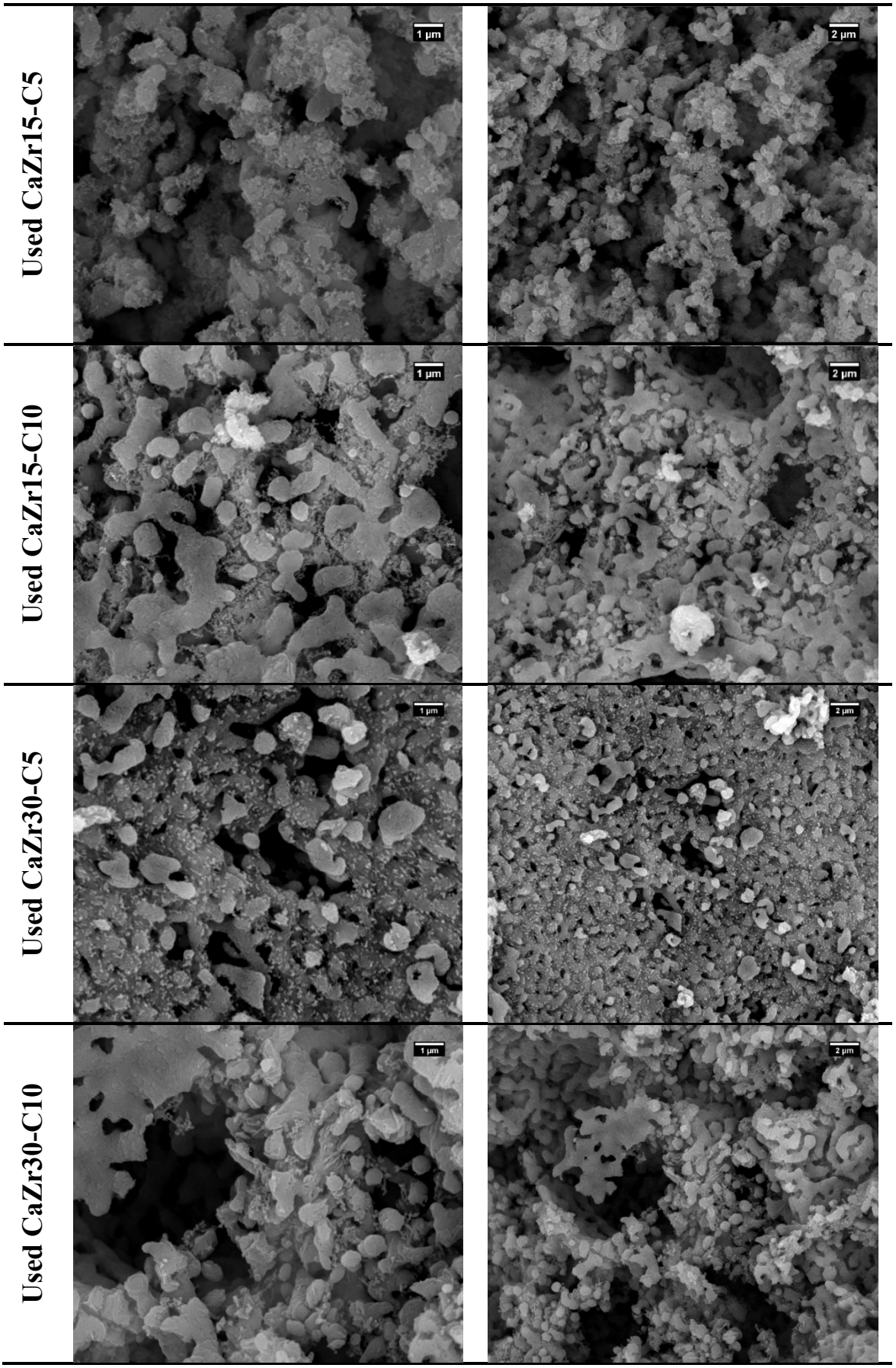
Used CaZr15-C5
Used CaZr15-C10
Used CaZr30-C5
Used CaZr30-C10
1 µm
2 µm

Fig. 8: SEM images of used CaZr15-C5, CaZr15-C10, CaZr30-C5, and CaZr30-C10, after processing during 15 cycles.

To quantitatively manifest the effect of CNT on the multicyclic performance of CaZr15-C0 and CaZr30-C0, the increment rates (%) in CO_2 capture capacity at the 15th cycle, CaO conversion at the 1st cycle, and the total amount of captured CO_2 by merging 2.5, 5, and 10 wt.% CNT with CaZr15-C0 and CaZr30-C0 are reported in **Fig. 9a** and **b**, respectively. There are outstanding improvements in the abovementioned characteristics when integrating with diverse CNT content. The most significant enhancements, including 41.74, 16.2, and 45.27 % in CO_2 capture capacity at the 15th cycle, CaO conversion at the 1st cycle, and the total amount of captured CO_2, are acquired by adding 5 wt.% CNT, respectively. Even though the most increase in CO_2 capture capacity of CaZr30-C0 at the 15th cycle, 49.5 %, is achieved in the case of CaZr30-C10, merging CaZr30-C0 with 5 wt.% CNT results in the highest enhancements in CaO conversion at the 1st cycle, 82.95 %, and the total amount of captured CO_2, 53.57 %.

The influence of BJH pore volume on CO_2 capture capacity at 15th cycles and the total amount of adsorbed CO_2 over 15 cycles exposed to severe CaL conditions is depicted in **Fig. 9c** and **d**. Merging CNT into Zr-stabilized CaO adsorbent raises BJH pore volume, affecting important multicyclic features. Enhancing BJH pore volume increases CO_2 capture capacity at the 15th cycle and the total amount of captured CO_2 over cycles. The highest CO_2 capture capacity at the 15th cycle of 0.164 g CO_2/g sorbent and the total amount of captured CO_2 of 2.92 g CO_2/g sorbent over 15 multiple cycles, are presented by CaZr15-C5, characterized with the highest BJH pore volume of 108.7 mm^3/g.

The relation between CaO crystallite size and the initial CaO conversion of all samples developed with Ca/Zr molar ratios of 15/1 and 30/1 are plotted in **Fig. 9e** and **f**, where CaO crystallite size inversely affects the initial CaO conversion. Sequentially, the highest initial

CaO conversion of 42.37% and 52.71% belongs to CaZr15-C5 and CaZr30-C5 with smaller CaO crystallite sizes of 22.3 and 19.8 nm. On the other hand, the lowest values of CaO conversion, 36.46 and 28.81 %, are reported for the CNT-free Zr-incorporated samples, CaZr15-C0 and CaZr30-C0, which possess giant CaO crystallite sizes of 26.5 and 29.6 nm, respectively. Developing CaO-adsorbents with smaller CaO grain sizes contributes to increasing the accessible CaO sites and, consequently, CaO conversion and CO_2 capture activity.

The role of BET surface area on the average sorption capacity of the 1st, 2^{nd,} and 3rd cycles for both clusters of synthesized adsorbents are depicted in **Fig. 9g** and h. A direct correlation between average sorption capacity and free surface area can be seen. Sequentially, sorbents with the highest and lowest average sorption capacity have the highest and lowest BET surface area. CaZr15-C5 and CaZr30-C5, with the maximum BET surface areas of 17.43 and 20.63 m^2/g, captured the higher amounts of CO_2 in their initial tricycles, 0.246 and 0.315 g CO_2/ g sorbent, respectively. Additionally, the minimum average sorption capacities of the 1st, 2^{nd,} and 3rd cycles are obtained for CaZr15-C0 and CaZr30-C0, potentially attributed to their minimum BET surface area.

Fig. 9i indicates the direct proportion between the BET surface area of used samples and ultimate sorption capacity, at the 15th cycle, with a correlation coefficient R^2 of 0.953. The used adsorbent with the highest BET surface area of 6.48 m^2/g is the CaZr15-C5, exhibiting the most sorption capacity of 0.164 g CO_2/ g sorbent at the final cycle. Due to the considerable sintering in inner layers of adsorbents after passing several cycles, the free surface area plays a crucial role in the sorption capacity of adsorbents. As a result, by simultaneous incorporation of 18.5 and 5 wt.% of $CaZrO_3$ and MWCNT into nanostructured CaO, the surface area value of used CaO increased by 155%, leading to an 86.4% increment in ultimate sorption capacity under harsh CaL condition.

Based on previous comprehensive structural and cyclic assessments, CaZr15-C5 and CaZr30-C5 are the best-developed samples. To directly compare CaZr15-C5 and CaZr30-C5, their CO_2 capture capacity and CaO conversion plots over 15 carbonation/calcination cycles under severe CaL conditions are presented in **Fig. 10a** and **b**, respectively. Due to the more CaO content, higher surface area, and pore volume, a higher amount of CO_2 is adsorbed in the case of CaZr30-C5 compared to CaZr15-C5. Nevertheless, the higher amount of thermal-resistance $CaZrO_3$ for CaZr15-C5 hinders the high-rate CaO sintering when CaO particles undergo several cycles under CaL conditions. More activation of CaZr15-C5, 60.52 %, arising from its higher $CaZrO_3$ content, is the main reason for its superior CO_2 capture capacity and CaO conversion from the 5^{th} cycle onwards compared to CaZr15-C5. However, the higher value of the total amount of captured CO_2 in the case of CaZr30-C5, 3.01 g CO_2/ g sorbent, than that of CaZr15-C5, 2.92 g CO_2/ g sorbent, can be attributed to its higher free CaO content of CaZr30-C5, 90 wt.%, compared to CaZr15-C5, 81.5 wt.%. The Ca/Zr molar ratio of 15/1 and CNT content of 5 wt.% are the most suitable preparation parameters.

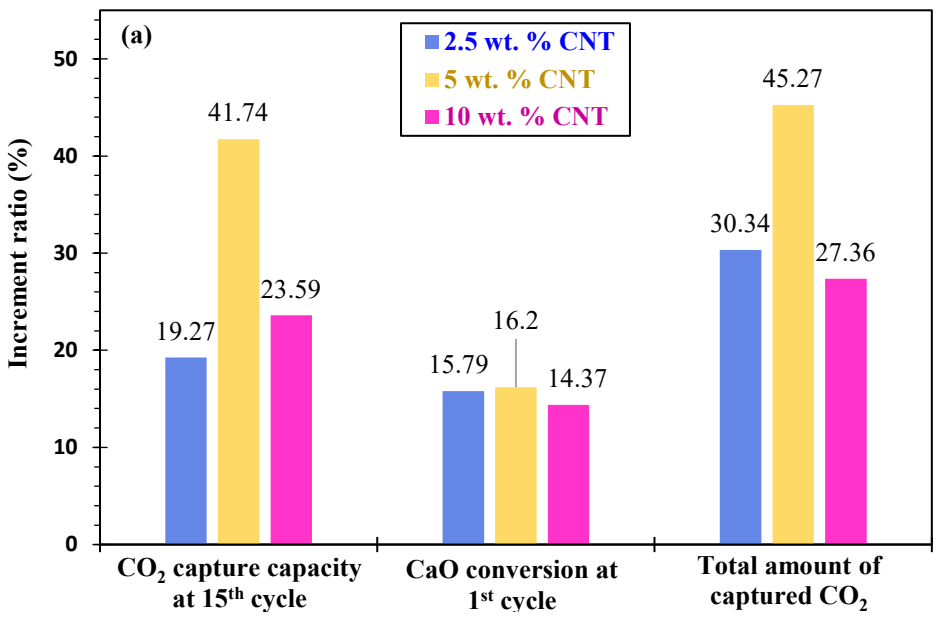
(a)
2.5 wt. % CNT
5 wt. % CNT
10 wt. % CNT
Increment ratio (%)
0
10
20
30
40
50
19.27
41.74
23.59
15.79
16.2
14.37
30.34
45.27
27.36
CO2 capture capacity at 15th cycle
CaO conversion at 1st cycle
Total amount of captured CO2

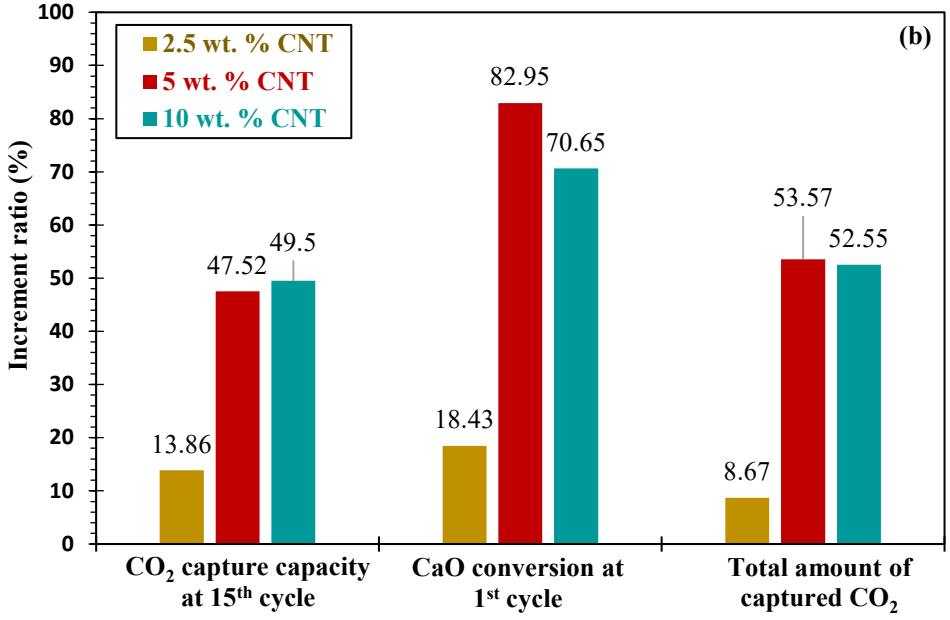
(b)
2.5 wt. % CNT
5 wt. % CNT
10 wt. % CNT
Increment ratio (%)
0
10
20
30
40
50
60
70
80
90
100
13.86
47.52
49.5
18.43
82.95
70.65
8.67
53.57
52.55
CO2 capture capacity at 15th cycle
CaO conversion at 1st cycle
Total amount of captured CO2

622

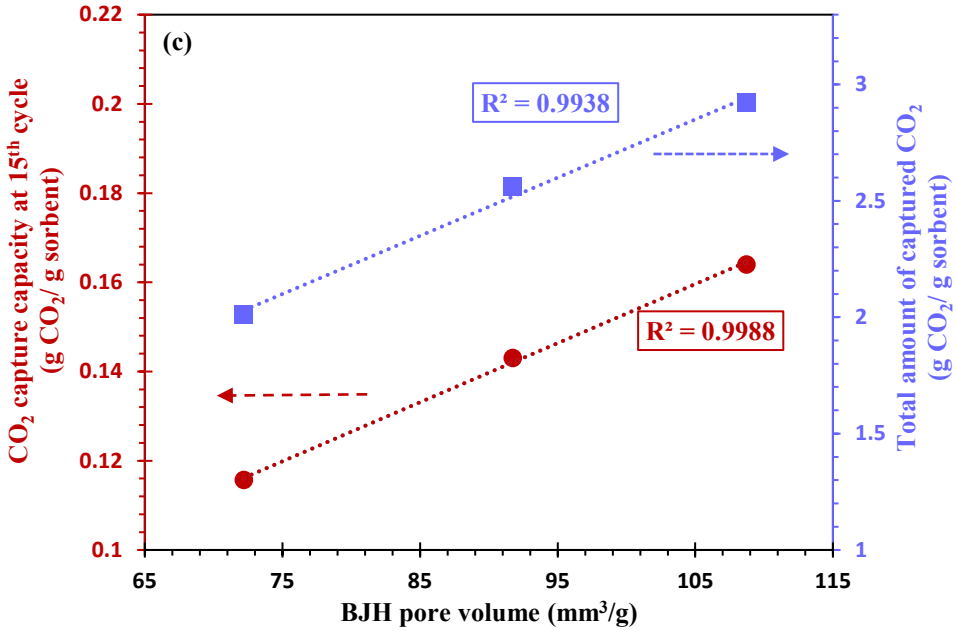
(c)
R² = 0.9938
R² = 0.9988
CO2 capture capacity at 15th cycle (g CO2/ g sorbent)
Total amount of captured CO2 (g CO2/ g sorbent)
0.1
0.12
0.14
0.16
0.18
0.2
0.22
1
1.5
2
2.5
3
65
75
85
95
105
115
BJH pore volume (mm3/g)

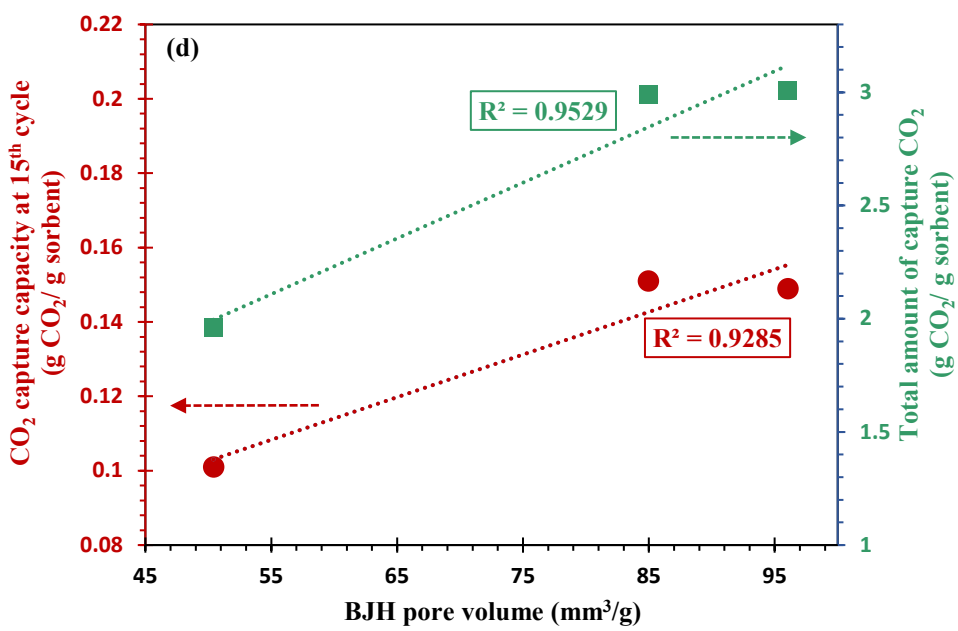
(d)
R² = 0.9529
R² = 0.9285
CO2 capture capacity at 15th cycle (g CO2/ g sorbent)
Total amount of capture CO2 (g CO2/ g sorbent)
0.08
0.1
0.12
0.14
0.16
0.18
0.2
0.22
1
1.5
2
2.5
3
45
55
65
75
85
95
BJH pore volume (mm3/g)

623

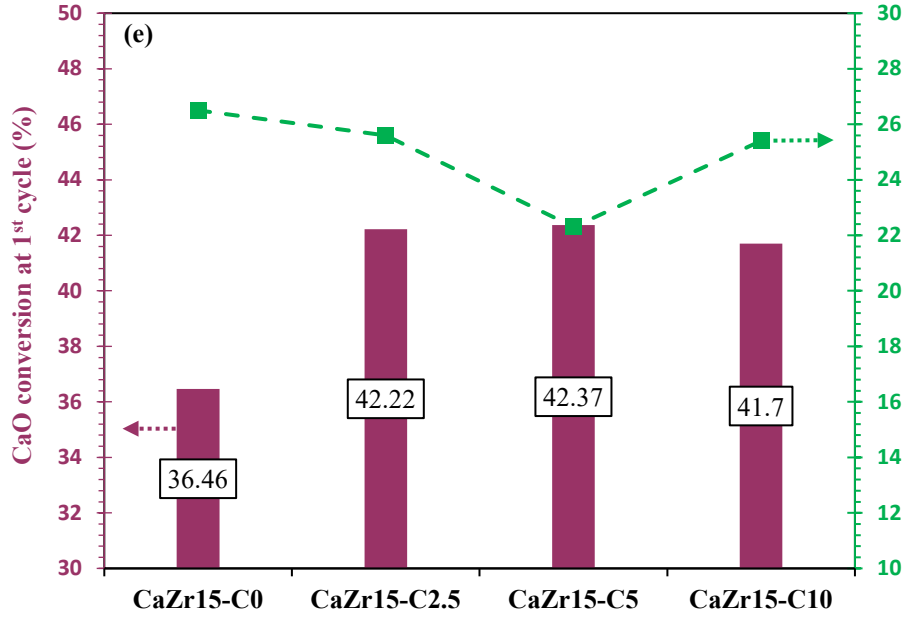
(e)
CaO conversion at 1st cycle (%)
CaO crystallite size (nm)
36.46
42.22
42.37
41.7
CaZr15-C0
CaZr15-C2.5
CaZr15-C5
CaZr15-C10

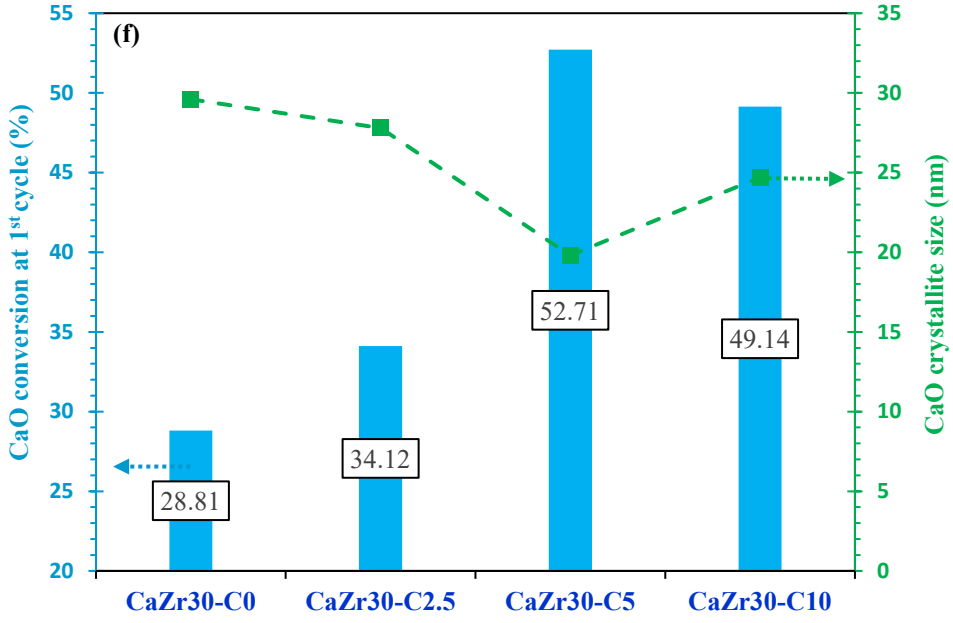
(f)
CaO conversion at 1st cycle (%)
CaO crystallite size (nm)
28.81
34.12
52.71
49.14
CaZr30-C0
CaZr30-C2.5
CaZr30-C5
CaZr30-C10

624

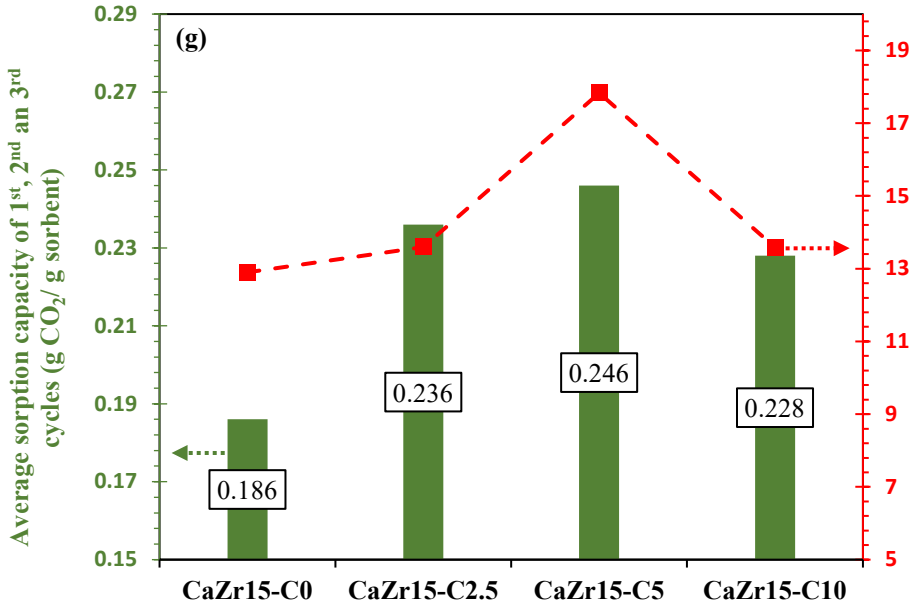
(g)
Average sorption capacity of 1st, 2nd an 3rd cycles (g CO2/ g sorbent)
BET surface area (m2/g)
0.186
0.236
0.246
0.228
CaZr15-C0
CaZr15-C2.5
CaZr15-C5
CaZr15-C10

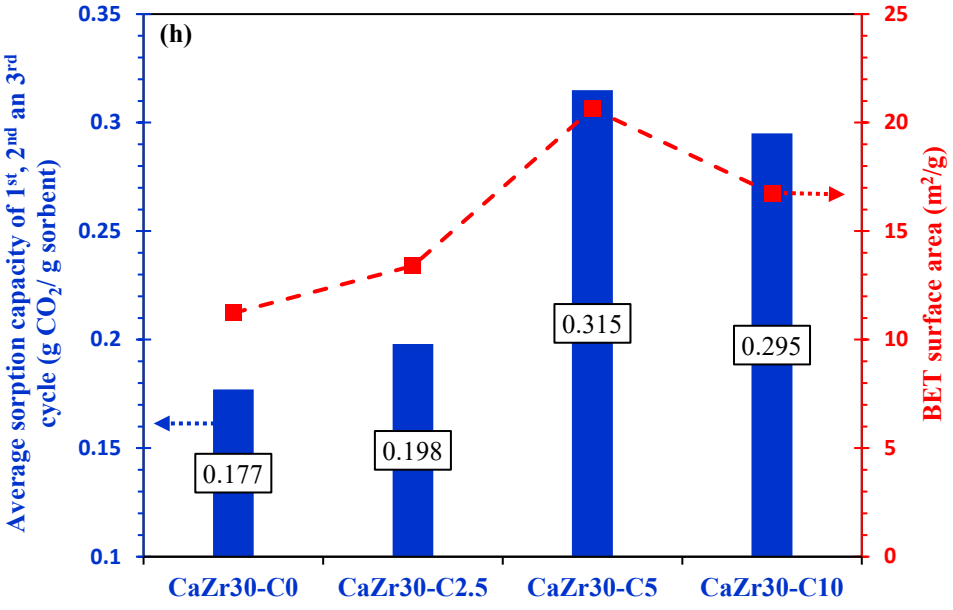
(h)
Average sorption capacity of 1st, 2nd an 3rd cycle (g CO2/ g sorbent)
BET surface area (m2/g)
0.177
0.198
0.315
0.295
CaZr30-C0
CaZr30-C2.5
CaZr30-C5
CaZr30-C10

625

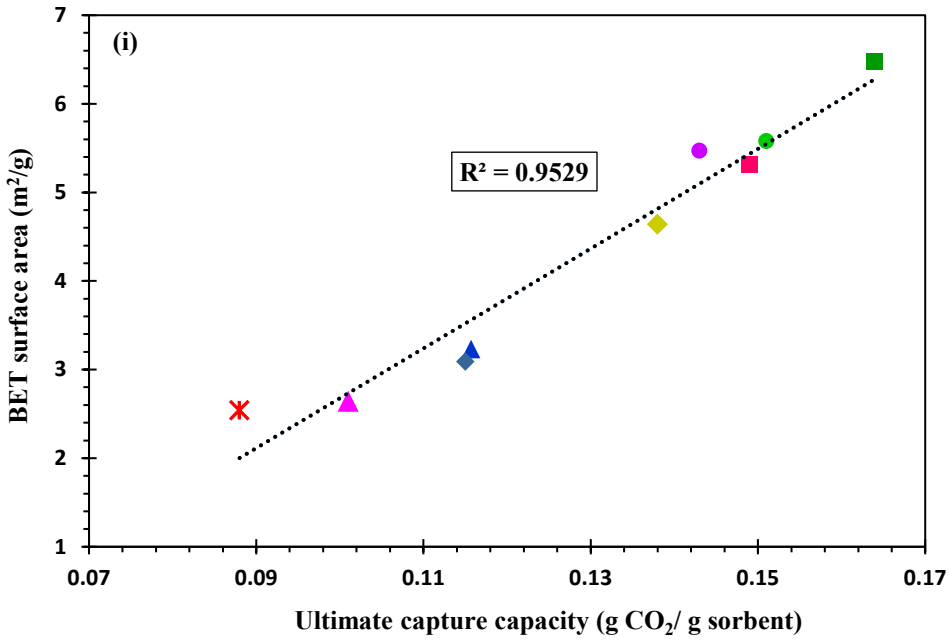

Fig. 9: Increment rate (%) of the total amount of captured CO_2, CaO conversion at 1st cycle, and CO_2 capture capacity at 15th cycle size by adding 2.5, 5, and 10 wt.% of CNT to (a) CaZr15-C0, and (b) CaZr30-C0, Total amount of captured CO_2 and CO_2 capture capacity at 15th cycle versus BJH pore volume for CNT-templated Zr-promoted CaO sorbents developed with Ca/Zr molar ratio of (c) 15/1, (d) 30/1, and CaZr30-C10, CaO conversion (%) at 1st cycle versus CaO crystallite size (nm) for CNT-templated Zr-promoted CaO sorbents developed with Ca/Zr molar ratio of (e) 15/1, (f) 30/1, mean sorption capacity at first three cycles versus BET surface area for CNT-templated Zr-promoted CaO sorbents developed with Ca/Zr molar ratio of (g) 15/1, (h) 30/1, (i) BET surface area value (m^2/g) of used samples versus ultimate sorption capacity at 15th cycles (g CO_2/ g sorbent)

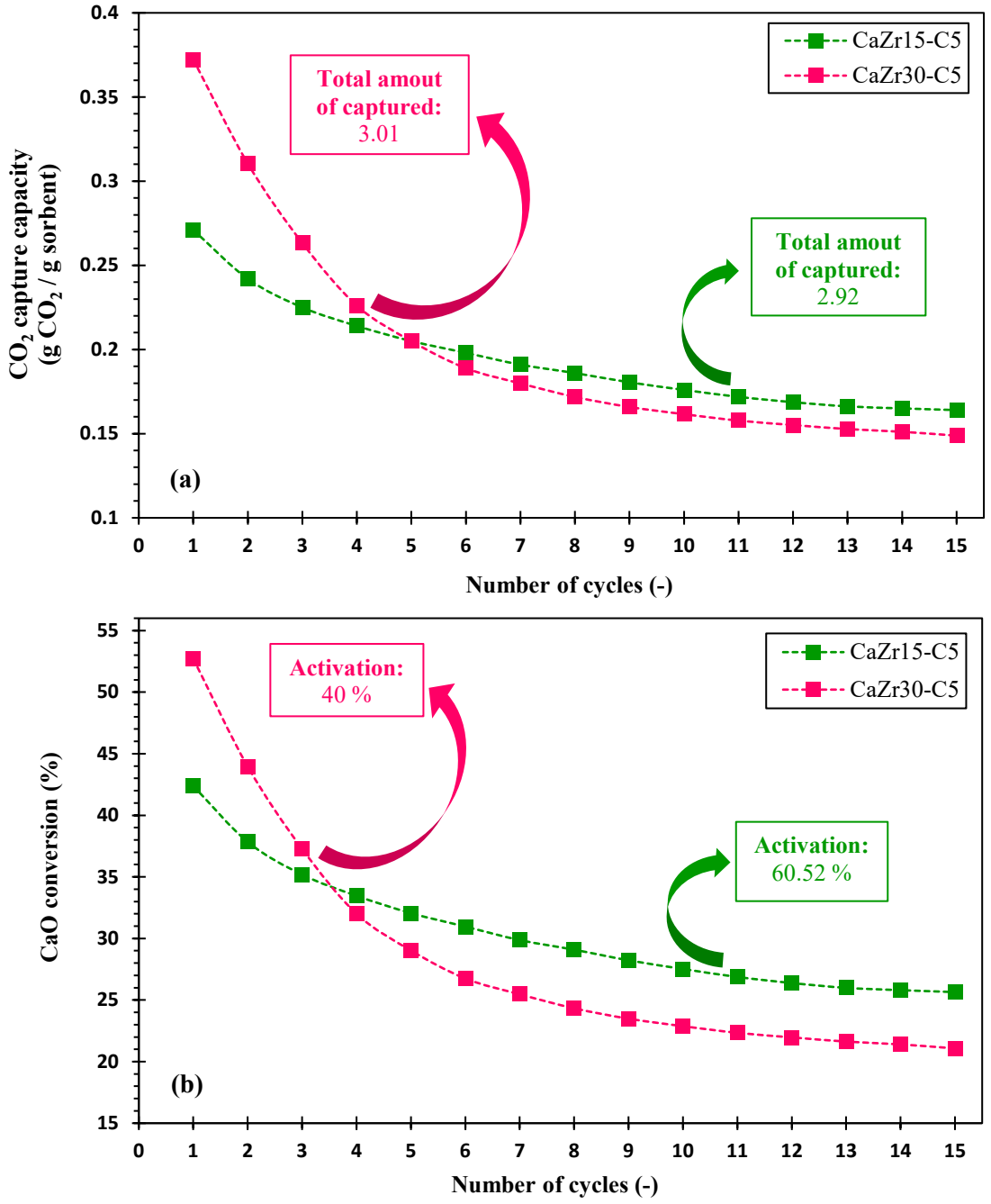

Fig. 10: Comparison of (a) CO_2 capture capacity and (b) CaO conversion of CaZr15-C5 and CaZr30-C5 during fifteen carbonation/calcination cycles under severe CaL conditions.

3.3. Outlook

Undeniable dependence of the CaL process on the applicability of CaO-based sorbents within fluidized bed reactors, including carbonator and calciner, under industrial process conditions, including short carbonation time and CO_2-rich calcination ambient, requires comprehensive assessments on scaling up cost-effective modified CaO-based sorbents in the

pilot-scale plants. Considering the economic aspects of the industrial CO_2 capture process, waste-material-derived CaO precursors, cost-effective thermal-resistance metal oxides, such as Al_2O_3 and MgO, and ubiquitous and affordable bio-based additives should be considered to develop CaO-based sorbents. Consequently, as our research's next target, we plan to conduct a thorough and detailed techno-economic investigation on the applicability of the biomaterials-incorporated durable-metal-promoted CaO sorbents derived from affordable ingredients into pilot-scale fluidized-bed reactors under industrial and realistic conditions in our forthcoming research.

4. Conclusion

The present research concentrates on improving the textural and structural properties and CO_2 adsorption performance of sol-gel-derived Zr-promoted CaO adsorbents containing minor $CaZrO_3$ contents by utilizing Multi-walled carbon nanotubes additive, for the first time in our knowledge. The Ca/Zr molar ratios of 15/1 and 30/1, and MWCNT concentrations of 2.5, 5, and 10 wt.% were employed to evaluate the effectiveness of MWCNT and determine the optimum parameters' values. The following worth noting outcomes can be presented:

1) The integration of 5 wt.% MWCNT, the best concentration based on textural and multicyclic results, into Zr-promoted CaO adsorbents, containing 10 and 18.5 wt.% $CaZrO_3$ resulted in the greatest improvements in textural and adsorptive features. For instance, 50.57 and 90.55% increments in pore volume, 38.1 and 83.7 increases in BET surface area, and 45.27 and 53.57% raises in the total amount of captured CO_2 over the 15 cycles CaL process reported for CaO developed with 15/1 and 30/1 molar ratios of Ca/Zr.
2) 5 wt.% CNT is the most efficient amount to significantly enhance the CO_2 capture activity of Zr-promoted CaO adsorbents containing a minor amount of $CaZrO_3$.

3) Combining CNT with Zr-modified CaO adsorbents homogenized the $CaZrO_3$ distribution into CaO texture.

4) Based on the multicyclic and textural data, MWCNT can be considered a remarkable candidate to compensate for the decreased amount of $CaZrO_3$, due to their drawbacks, for preparing highly durable CaO adsorbent.

Author contribution:

Mohammad Heidari: Investigation, Project administration, Conceptualization, Methodology, Formal analysis, Writing original draft. **Seyed Borhan Mousavi:** Investigation, Methodology, Conceptualization, Formal analysis, Writing original draft. **Farhad Rahmani:** Supervision, Project administration, Visualization, Conceptualization, Review & Editing. **Peter Clough:** Review & Editing. **Serap Ozmen:** Investigation.

References:

1. Zhang Z X, Xu H J, Hua W S, Zhao C Y. Thermodynamics analysis of multi-stage temperature swing adsorption cycle for dilute CO_2 capture, enrichment and purification. Energy Conversion and Management, 2022, 265: 115794.
2. Ashrafi M, Mousavi S B, Zeinali Heris S, Heidari M, Mohammadpourfard M, Aslani H. Investigation of H_2O_2/UV advanced oxidation process on the removal rate of coliforms from the industrial effluent: A pilot-scale study. International Journal of Hydrogen Energy, 2022.
3. Li Y, Wang N, Guan H, Jia Z, Zhang Y, Zhao G, Gao M. Optimization study of CO_2 capture unit for subcritical coal-fired power generation unit based on Ebsilon and Aspen plus. Energy Conversion and Management, 2022, 269: 116111.
4. Ali Abd A, Jihad Kadhim Shabbani H, Helwani Z, Roslee Othman M. Novel design of pressure swing adsorption using compact plates for adsorption heat recuperation of CO_2 capture in biomethane upgrading process. Energy Conversion and Management, 2022, 268: 115999.
5. Cheng F, Small A A, Colosi L M. The levelized cost of negative CO_2 emissions from thermochemical conversion of biomass coupled with carbon capture and storage. Energy Conversion and Management, 2021, 237: 114115.
6. Choi S, Moon H, Bang M, Kim K, Park Y-K, Cho H H. Efficient design of heat exchange for CFB reactors in CO_2 capture system regarding geometry-induced secondary flow. Energy Conversion and Management, 2021, 235: 113995.
7. Sun Y, Dong B, Wang L, Li H, Thorin E. Technology selection for capturing CO_2 from wood pyrolysis. Energy Conversion and Management, 2022, 266: 115835.
8. Xiang D, Li P, Yuan X. Energy consumption and CO_2 emissions of petroleum coke-to-methanol with/without carbon capture using process modeling and life cycle analysis. Energy Conversion and Management, 2021, 248: 114823.
9. Alibrahim H A, Khalafalla S S, Ahmed U, Park S, Lee C-J, Zahid U. Conceptual design of syngas production by the integration of gasification and dry-reforming technologies with CO_2 capture and utilization. Energy Conversion and Management, 2021, 244: 114485.
10. del Pozo C A, Cloete S, Álvaro Á J. Carbon-negative hydrogen: Exploring the techno-economic potential of biomass co-gasification with CO_2 capture. Energy Conversion and Management, 2021, 247: 114712.
11. Oh H-T, Kum J, Park J, Dat Vo N, Kang J-H, Lee C-H. Pre-combustion CO_2 capture using amine-based absorption process for blue H_2 production from steam methane reformer. Energy Conversion and Management, 2022, 262: 115632.
12. Khallaghi N, Abbas S Z, Manzolini G, De Coninck E, Spallina V. Techno-economic assessment of blast furnace gas pre-combustion decarbonisation integrated with the power generation. Energy Conversion and Management, 2022, 255: 115252.
13. Szima S, Arnaiz del Pozo C, Cloete S, Chiesa P, Jiménez Alvaro Á, Cormos A-M, Amini S. Finding synergy between renewables and coal: Flexible power and hydrogen production from advanced IGCC plants with integrated CO_2 capture. Energy Conversion and Management, 2021, 231: 113866.
14. Serrano J R, Martín J, Gomez-Soriano J, Raggi R. Theoretical and experimental evaluation of the spark-ignition premixed oxy-fuel combustion concept for future CO_2 captive powerplants. Energy Conversion and Management, 2021, 244: 114498.
15. Serrano J R, Arnau F J, García-Cuevas L M, Farias V H. Oxy-fuel combustion feasibility of compression ignition engines using oxygen separation membranes for

enabling carbon dioxide capture. Energy Conversion and Management, 2021, 247: 114732.
16. Wu Y, Dai Y, Xie W, Chen H, Zhu Y. System integration for combined heat and power (CHP) plants with post-combustion CO_2 capture. Energy Conversion and Management, 2022, 258: 115508.
17. Mosaffa A Farshi L G. Novel post combustion CO_2 capture in the coal-fired power plant employing a transcritical CO_2 power generation and low temperature steam upgraded by an absorption heat transformer. Energy Conversion and Management, 2020, 207: 112542.
18. Asadi J Kazempoor P. Techno-economic analysis of membrane-based processes for flexible CO_2 capturing from power plants. Energy Conversion and Management, 2021, 246: 114633.
19. Akrami E, Ameri M, Rocco M V. Integration of biomass-fueled power plant and MCFC-cryogenic CO_2 separation unit for low-carbon power production: Thermodynamic and exergoeconomic comparative analysis. Energy Conversion and Management, 2020, 223: 113304.
20. Kim S, Lee J W, Choi H W, Lee G J, Xu R, Yoon S H, Xu Z, Wang R, Tae Kang Y. CO_2 capture-driven thermal battery using functionalized solvents for plus energy building application. Energy Conversion and Management, 2022, 260: 115606.
21. Nobarzad M J, Tahmasebpoor M, Heidari M, Pevida C. Theoretical and experimental study on the fluidity performance of hard-to-fluidize carbon nanotubes-based CO_2 capture sorbents. Frontiers of Chemical Science and Engineering, 2022.
22. Adnan M A, Pradiptya I, Haque T I, Hossain M M. Integrated diesel fueled chemical looping combustion for power generation and CO_2 capture – Performance evaluation based on exergy analysis. Energy Conversion and Management, 2020, 206: 112430.
23. Tregambi C, Bareschino P, Mancusi E, Pepe F, Montagnaro F, Solimene R, Salatino P. Modelling of a concentrated solar power – photovoltaics hybrid plant for carbon dioxide capture and utilization via calcium looping and methanation. Energy Conversion and Management, 2021, 230: 113792.
24. Colelli G, Chacartegui R, Ortiz C, Carro A, Arena A P, Verda V. Life cycle and environmental assessment of calcium looping (CaL) in solar thermochemical energy storage. Energy Conversion and Management, 2022, 257: 115428.
25. Liu G, Zhao Y, Heberlein S, Veksha A, Giannis A, Ping Chan W, Thye Lim T, Lisak G. Hydrogen and power co-production from autothermal biomass sorption enhanced chemical looping gasification: Thermodynamic modeling and comparative study. Energy Conversion and Management, 2022, 269: 116087.
26. Xu Y, Zhang T, Lu B, Luo C, Wu F, Li X, Zhang L. Glycine tailored effective CaO-based heat carriers for thermochemical energy storage in concentrated solar power plants. Energy Conversion and Management, 2021, 250: 114886.
27. Zhang C, Li Y, Yang L, Fan X, Chu L. Analysis on H_2 production process integrated $CaO/Ca(OH)_2$ heat storage and sorption enhanced staged gasification using calcium looping. Energy Conversion and Management, 2022, 253: 115169.
28. Heidari M, Tahmasebpoor M, Antzaras A, Lemonidou A A. CO_2 capture and fluidity performance of CaO-based sorbents: Effect of Zr, Al and Ce additives in tri-, bi- and mono-metallic configurations. Process Safety and Environmental Protection, 2020, 144: 349-365.
29. Heidari M, Tahmasebpoor M, Mousavi S B, Pevida C. CO_2 capture activity of a novel CaO adsorbent stabilized with $(ZrO_2+Al_2O_3+CeO_2)$-based additive under mild and realistic calcium looping conditions. Journal of CO_2 Utilization, 2021, 53: 101747.

30. Mousavi S B, Zeinali Heris S, Estellé P. Viscosity, tribological and physicochemical features of ZnO and MoS2 diesel oil-based nanofluids: An experimental study. Fuel, 2021, 293: 120481.
31. Seyedi S S, Shabgard M R, Mousavi S B, Zeinali Heris S. The impact of SiC, Al_2O_3, and B_2O_3 abrasive particles and temperature on wear characteristics of 18Ni (300) maraging steel in abrasive flow machining (AFM). International Journal of Hydrogen Energy, 2021, 46(68): 33991-34001.
32. Yahyavi S R, Haghighi M, Shafiei S, Abdollahifar M, Rahmani F. Ultrasound-assisted synthesis and physicochemical characterization of Ni–Co/Al_2O_3–MgO nanocatalysts enhanced by different amounts of MgO used for CH_4/CO_2 reforming. Energy Conversion and Management, 2015, 97: 273-281.
33. Rahmani F Haghighi M. One-pot hydrothermal synthesis of ZSM-5–CeO_2 composite as a support for Cr-based nanocatalysts: influence of ceria loading and process conditions on CO_2-enhanced dehydrogenation of ethane. RSC Advances, 2016, 6(92): 89551-89563.
34. Rahmani F Haghighi M. C_2H_6/CO_2 oxidative dehydrogenation (ODH) reaction on nanostructured CrAPSO-34 catalyst: One-pot hydrothermal vs. conventional hydrothermal/impregnation catalyst synthesis. Korean Journal of Chemical Engineering, 2016, 33(9): 2555-2566.
35. Hu Y, Lu H, Liu W, Yang Y, Li H. Incorporation of CaO into inert supports for enhanced CO_2 capture: A review. Chemical Engineering Journal, 2020, 396: 125253.
36. Radfarnia H R Iliuta M C. Metal oxide-stabilized calcium oxide CO_2 sorbent for multicycle operation. Chemical Engineering Journal, 2013, 232: 280-289.
37. Antzara A N, Arregi A, Heracleous E, Lemonidou A A. In-depth evaluation of a ZrO_2 promoted CaO-based CO_2 sorbent in fluidized bed reactor tests. Chemical Engineering Journal, 2018, 333: 697-711.
38. Yoon H J Lee K B. Introduction of chemically bonded zirconium oxide in CaO-based high-temperature CO_2 sorbents for enhanced cyclic sorption. Chemical Engineering Journal, 2019, 355: 850-857.
39. Armutlulu A, Naeem M A, Liu H J, Kim S M, Kierzkowska A, Fedorov A, Müller C R. Multishelled CaO microspheres stabilized by atomic layer deposition of Al_2O_3 for enhanced CO_2 capture performance. Advanced Materials, 2017, 29(41): 1702896.
40. Naeem M A, Armutlulu A, Imtiaz Q, Donat F, Schäublin R, Kierzkowska A, Müller C R. Optimization of the structural characteristics of CaO and its effective stabilization yield high-capacity CO_2 sorbents. Nature communications, 2018, 9(1): 1-11.
41. Kim S M, Armutlulu A, Kierzkowska A M, Müller C R. Inverse opal-like, $Ca_3Al_2O_6$-stabilized, CaO-based CO_2 sorbent: stabilization of a highly porous structure to improve its cyclic CO_2 uptake. ACS Applied Energy Materials, 2019, 2(9): 6461-6471.
42. Javadpour R, Zeinali Heris S, Mohammadfam Y. Optimizing the effect of concentration and flow rate of water/ MWCNTs nanofluid on the performance of a forced draft cross-flow cooling tower. Energy, 2021, 217: 119420.
43. Javadpour R, Heris S Z, Mohammadfam Y, Mousavi S B. Optimizing the heat transfer characteristics of MWCNTs and TiO_2 water-based nanofluids through a novel designed pilot-scale setup. Scientific Reports, 2022, 12(1): 15154.
44. Karimi Bakhtiyar N, Javadpour R, Zeinali Heris S, Mohammadpourfard M. Improving the thermal characteristics of a cooling tower by replacing the operating fluid with functionalized and non-functionalized aqueous MWCNT nanofluids. Case Studies in Thermal Engineering, 2022, 39: 102422.

45. Javadpour R, Zeinali Heris S, Meyer J P. Experimental study of the effect of filled bed type on the performance of a cross-flow cooling tower with the approach of using nanofluids. Energy Reports, 2022, 8: 8346-8360.
46. Aghaei Sarvari A, Zeinali Heris S, Mohammadpourfard M, Mousavi S B, Estellé P. Numerical investigation of TiO_2 and MWCNTs turbine meter oil nanofluids: Flow and hydrodynamic properties. Fuel, 2022, 320: 123943.
47. Yao Y, Lian C, Wu G, Hu Y, Wei F, Yu M, Wang S. Synthesis of "sea urchin"-like carbon nanotubes/porous carbon superstructures derived from waste biomass for treatment of various contaminants. Applied Catalysis B: Environmental, 2017, 219: 563-571.
48. Wang G, Deng Y, Yu J, Zheng L, Du L, Song H, Liao S. From chlorella to nestlike framework constructed with doped carbon nanotubes: a biomass-derived, high-performance, bifunctional oxygen reduction/evolution catalyst. ACS applied materials & interfaces, 2017, 9(37): 32168-32178.
49. Zhang Y, Lu L, Zhang S, Lv Z, Yang D, Liu J, Chen Y, Tian X, Jin H, Song W. Biomass chitosan derived cobalt/nitrogen doped carbon nanotubes for the electrocatalytic oxygen reduction reaction. Journal of Materials Chemistry A, 2018, 6(14): 5740-5745.
50. Osman A I, Blewitt J, Abu-Dahrieh J K, Farrell C, Al-Muhtaseb A a H, Harrison J, Rooney D W. Production and characterisation of activated carbon and carbon nanotubes from potato peel waste and their application in heavy metal removal. Environmental science and pollution research, 2019, 26(36): 37228-37241.
51. Yang M, Yuan Y, Li Y, Sun X, Wang S, Liang L, Ning Y, Li J, Yin W, Che R. Dramatically enhanced electromagnetic wave absorption of hierarchical CNT/Co/C fiber derived from cotton and metal-organic-framework. Carbon, 2020, 161: 517-527.
52. Zhou S, Zhang B, Liao Z, Zhou L, Yuan Y. Autochthonous N-doped carbon nanotube/activated carbon composites derived from industrial paper sludge for chromate (VI) reduction in microbial fuel cells. Science of the Total Environment, 2020, 712: 136513.
53. Wang Z, Ogata H, Morimoto S, Ortiz-Medina J, Fujishige M, Takeuchi K, Muramatsu H, Hayashi T, Terrones M, Hashimoto Y. Nanocarbons from rice husk by microwave plasma irradiation: From graphene and carbon nanotubes to graphenated carbon nanotube hybrids. Carbon, 2015, 94: 479-484.
54. Fathy N A. Carbon nanotubes synthesis using carbonization of pretreated rice straw through chemical vapor deposition of camphor. RSC advances, 2017, 7(45): 28535-28541.
55. Reva V, Filatenkov A, Yagofarov V, Gulevskii D, Kuryavyi V, Mansurov Y N. Analysis of the Formation of Multi-Layer Carbon Nanotubes in the Process of Mechanical Activation of the Pyrolysis Products of Vegetable Raw Materials. in IOP Conference Series: Materials Science and Engineering. 2016. IOP Publishing.
56. Mousavi S B, Heris S Z, Estellé P. Experimental comparison between ZnO and MoS_2 nanoparticles as additives on performance of diesel oil-based nano lubricant. Scientific reports, 2020, 10(1): 1-17.
57. Mousavi S B, Zeinali Heris S, Hosseini M G. Experimental investigation of MoS_2/diesel oil nanofluid thermophysical and rheological properties. International Communications in Heat and Mass Transfer, 2019, 108: 104298.
58. Mousavi S B Zeinali Heris S. Experimental investigation of ZnO nanoparticles effects on thermophysical and tribological properties of diesel oil. International Journal of Hydrogen Energy, 2020, 45(43): 23603-23614.

59. Antzara A, Heracleous E, Lemonidou A A. Improving the stability of synthetic CaO-based CO_2 sorbents by structural promoters. Applied energy, 2015, 156: 331-343.
60. Jing J-y, Li T-y, Zhang X-w, Wang S-d, Feng J, Turmel W A, Li W-y. Enhanced CO_2 sorption performance of $CaO/Ca_3Al_2O_6$ sorbents and its sintering-resistance mechanism. Applied Energy, 2017, 199: 225-233.
61. Lazaro A, Brouwers H, Quercia G, Geus J. The properties of amorphous nano-silica synthesized by the dissolution of olivine. Chemical Engineering Journal, 2012, 211: 112-121.
62. Naghash-Hamed S, Arsalani N, Mousavi S B. Facile copper ferrite/carbon quantum dots magnetic nanocomposite as an effective nitro group reduction reaction nano catalyst for reduction of Para-nitroaniline and Ortho-nitroaniline. Nano Futures, 2022.
63. Naghash-Hamed S, Arsalani N, Mousavi S B. The catalytic reduction of nitroanilines using synthesized $CuFe_2O_4$ nanoparticles in an aqueous medium. ChemistryOpen, 2022.
64. Thommes M, Kaneko K, Neimark A V, Olivier J P, Rodriguez-Reinoso F, Rouquerol J, Sing K S. Physisorption of gases, with special reference to the evaluation of surface area and pore size distribution (IUPAC Technical Report). Pure and applied chemistry, 2015, 87(9-10): 1051-1069.
65. Yan F, Jiang J, Chen X, Tian S, Li K. Synthesis and characterization of silica nanoparticles preparing by low-temperature vapor-phase hydrolysis of SiCl4. Industrial & Engineering Chemistry Research, 2014, 53(30): 11884-11890.
66. Yan F, Jiang J, Li K, Liu N, Chen X, Gao Y, Tian S. Green synthesis of nanosilica from coal fly ash and its stabilizing effect on CaO sorbents for CO_2 capture. Environmental science & technology, 2017, 51(13): 7606-7615.
67. Sing K S. Reporting physisorption data for gas/solid systems with special reference to the determination of surface area and porosity (Recommendations 1984). Pure and applied chemistry, 1985, 57(4): 603-619.
68. Delir Kheyrollahi Nezhad P, Haghighi M, Rahmani F. CO_2/O_2-enhanced ethane dehydrogenation over a sol–gel synthesized Ni/ZrO2–MgO nanocatalyst: Effects of Mgo, ZrO_2, and NiO on the catalytic performance. Particulate Science and Technology, 2018, 36(8): 1017-1028.
69. Delir Kheyrollahi Nezhad P, Haghighi M, Jodeiri N, Rahmani F. Sol–gel preparation of NiO/ZrO2(x)–MgO(100−x) nanocatalyst used in CO_2/O_2 oxidative dehydrogenation of ethane to ethylene: influence of Mg/Zr ratio on catalytic performance. Journal of Sol-Gel Science and Technology, 2016, 80(2): 436-450.
70. Rahmani F, Haghighi M, Mohammadkhani B. Enhanced dispersion of Cr nanoparticles over nanostructured ZrO_2-doped ZSM-5 used in CO_2-oxydehydrogenation of ethane. Microporous and Mesoporous Materials, 2017, 242: 34-49.

The novel Carbon Nanotune-assisted development of highly porous $CaZrO_3$-CaO xerogel with boosted sorption activity towards high-temperature cyclic CO_2 capture

Mohammad Heidari [a,b], *Seyed Borhan Mousavi* [c], *Farhad Rahmani* [b,*], *Peter T. Clough* [d], *Serap Ozmen* [d]

[a] Faculty of Chemical & Petroleum Engineering, University of Tabriz, Tabriz, Iran

[b] Department of Chemical Engineering, Faculty of Engineering, University of Kurdistan, Sanandaj, P.O.Box 66177-15175, Iran

[c] J. Mike Walker '66 Mechanical Engineering Department, Texas A&M University, College Station, TX, USA

[d] Energy and Power Theme, School of Water, Energy and Environment, Cranfield University, Bedford, Bedfordshire, MK43 0AL, UK

[*] Corresponding Author.
Email address: F.rahmanichiyane@uok.ac.ir

Result and discussion:

Characterization

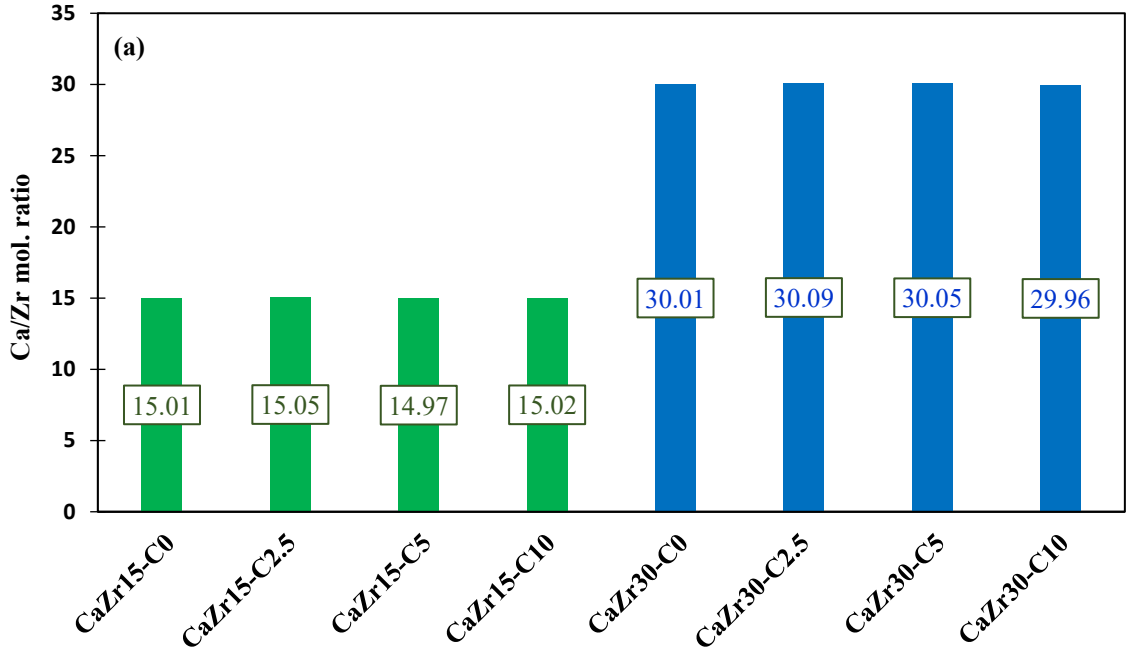

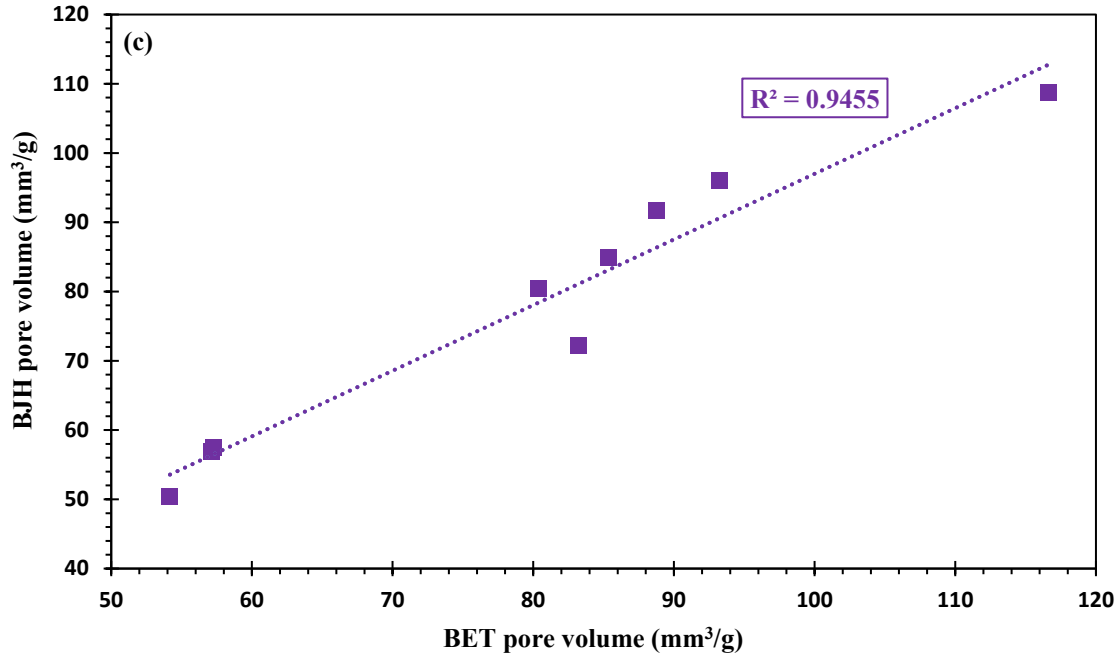

Fig. S1: (a) Ca/Zr molar ratio derived from ICP analysis of all developed Zr-decorated CaO-based xerogels, and **(c)** BJH pore volume versus BET pore volume for all synthesized CaO-based sorbents.

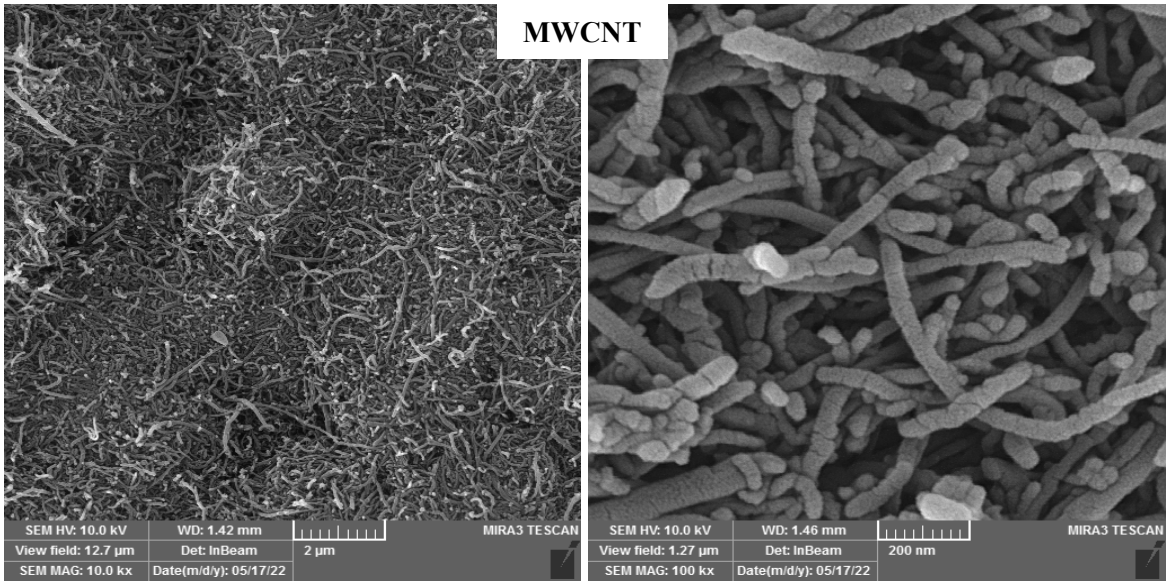
MWCNT
SEM HV: 10.0 kV
WD: 1.42 mm
MIRA3 TESCAN
View field: 12.7 µm
Det: InBeam
2 µm
SEM MAG: 10.0 kx
Date(m/d/y): 05/17/22
SEM HV: 10.0 kV
WD: 1.46 mm
MIRA3 TESCAN
View field: 1.27 µm
Det: InBeam
200 nm
SEM MAG: 100 kx
Date(m/d/y): 05/17/22

21

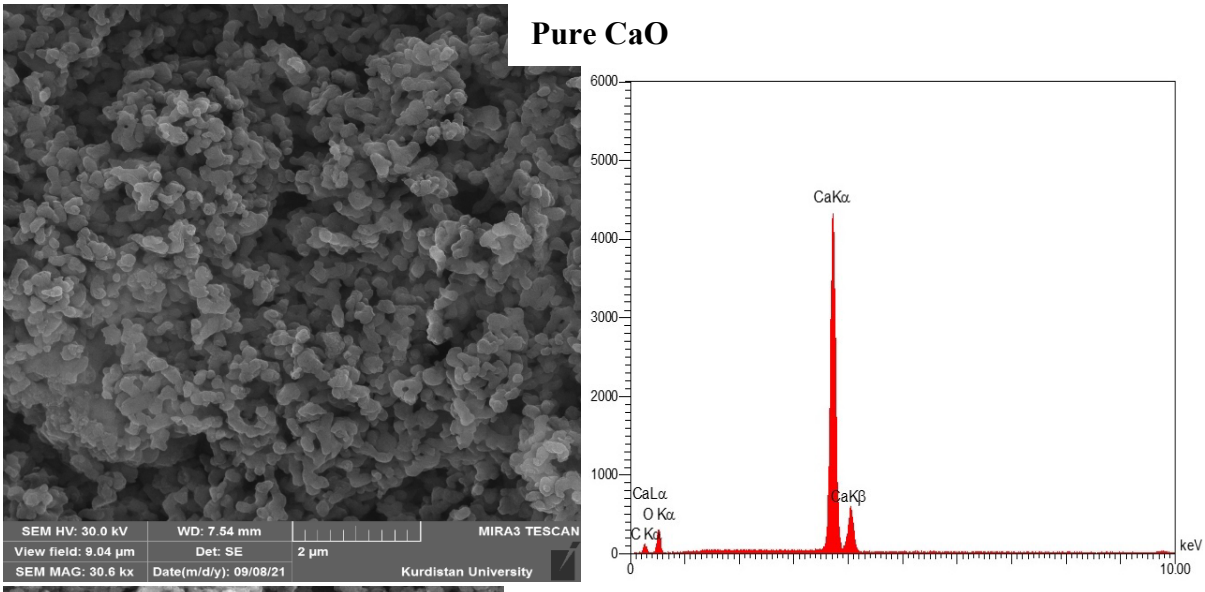
Pure CaO
SEM HV: 30.0 kV
WD: 7.54 mm
MIRA3 TESCAN
View field: 9.04 µm
Det: SE
2 µm
SEM MAG: 30.6 kx
Date(m/d/y): 09/08/21
Kurdistan University
6000
5000
4000
3000
2000
1000
0
CaKα
CaLα
O Kα
C Kα
CaKβ
keV
0
10.00

22

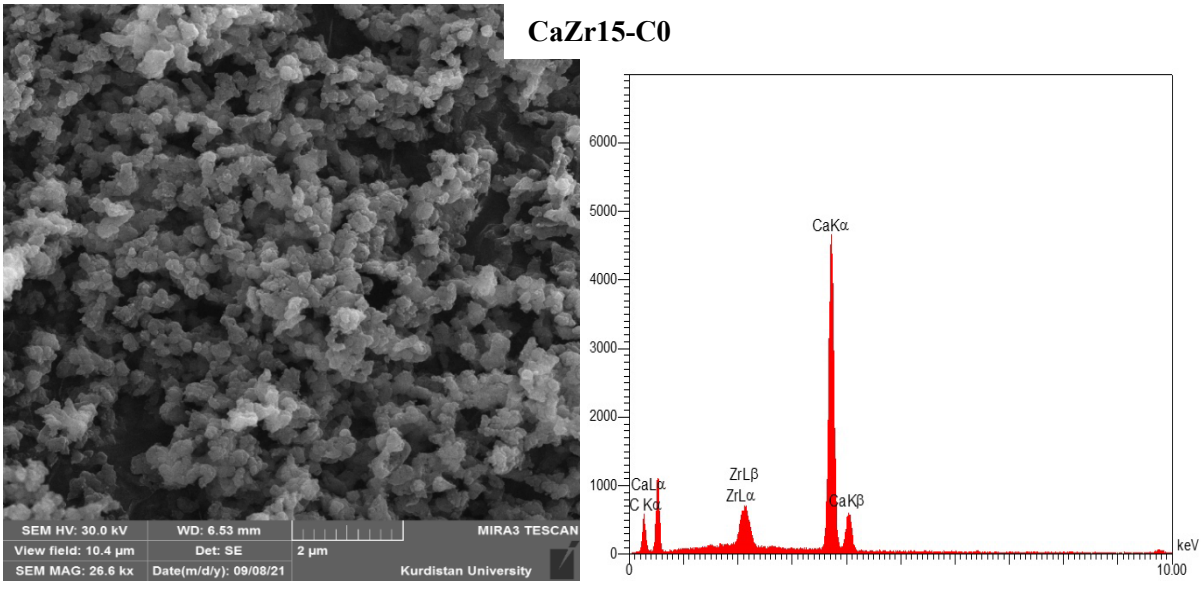
CaZr15-C0
SEM HV: 30.0 kV
WD: 6.53 mm
MIRA3 TESCAN
View field: 10.4 µm
Det: SE
2 µm
SEM MAG: 26.6 kx
Date(m/d/y): 09/08/21
Kurdistan University
6000
5000
4000
3000
2000
1000
0
CaKα
CaLα
C Kα
ZrLβ
ZrLα
CaKβ
keV
0
10.00

23

CaZr15-C2.5

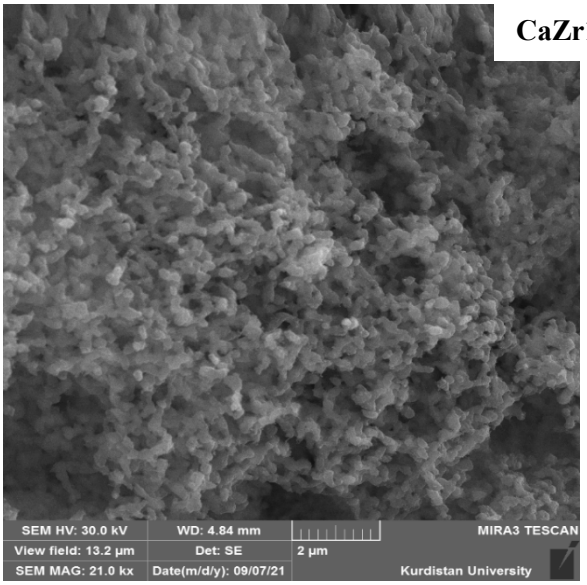

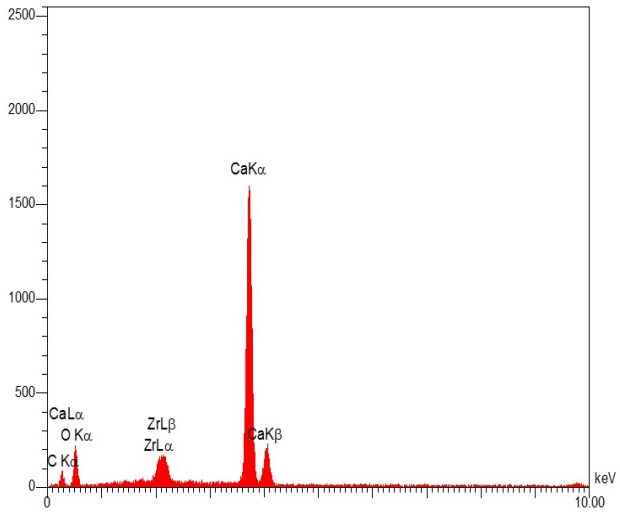

24

CaZr15-C5

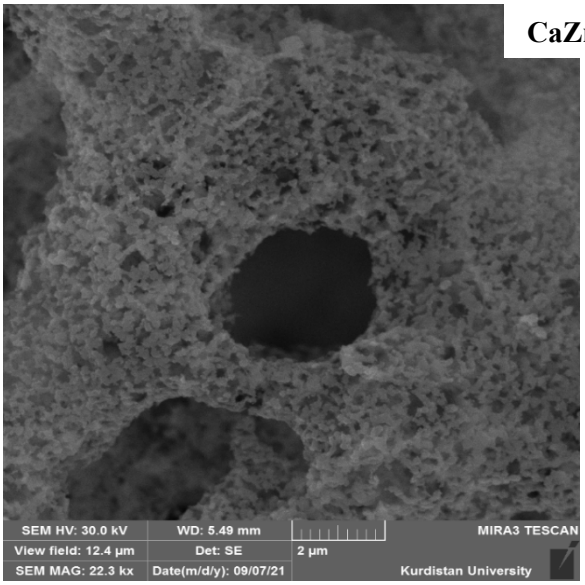

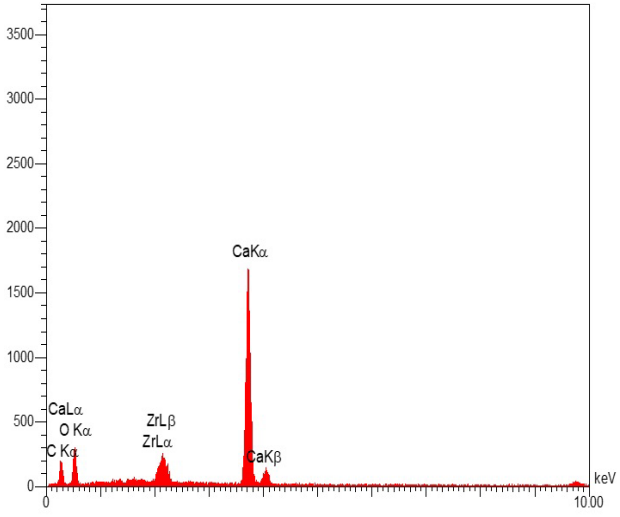

25

CaZr15-C10

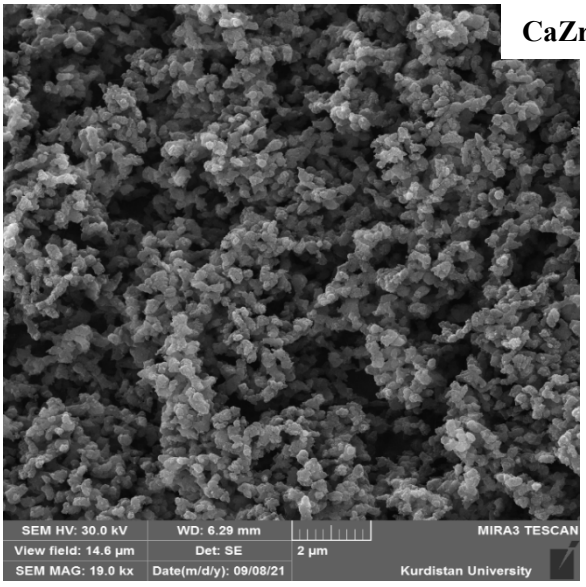

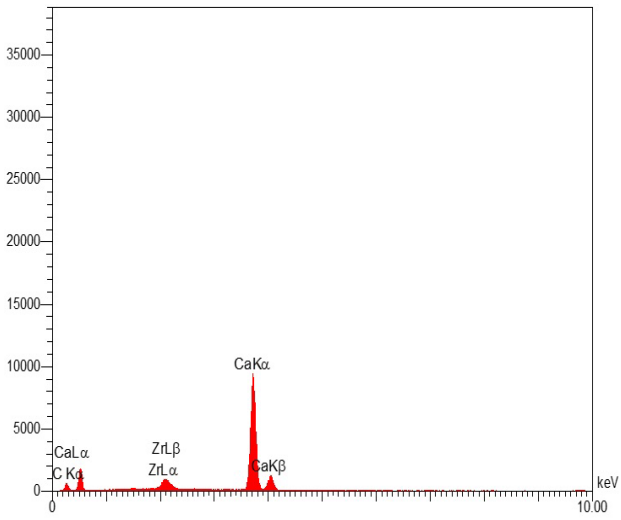

26

CaZr30-C0

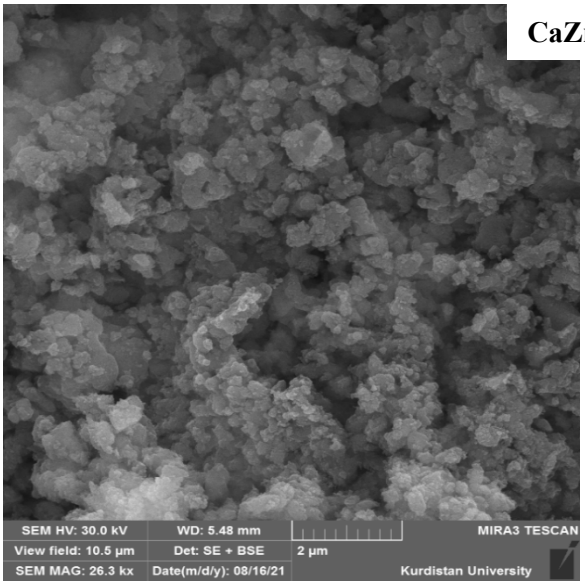

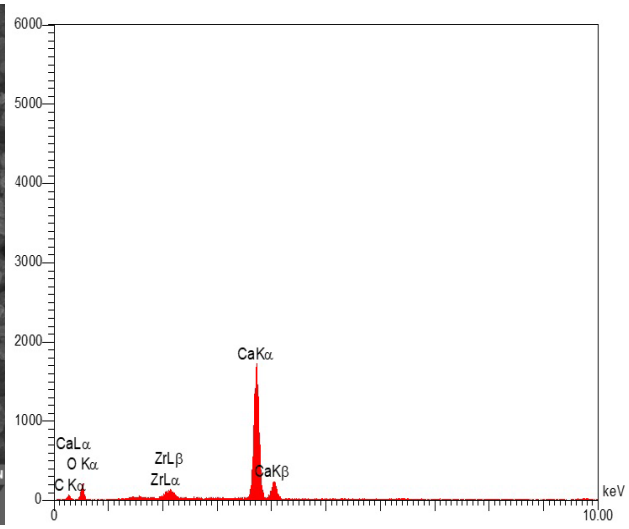

27

CaZr30-C2.5

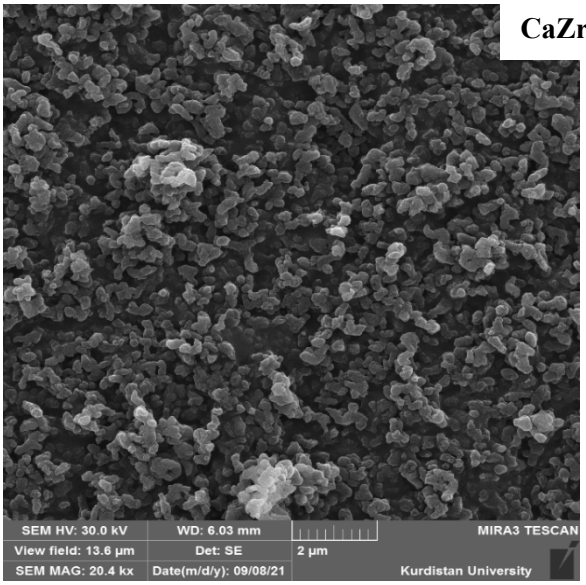

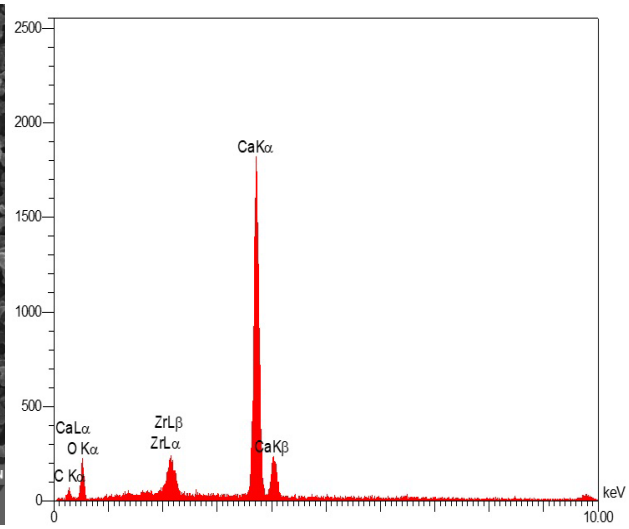

28

CaZr30-C5

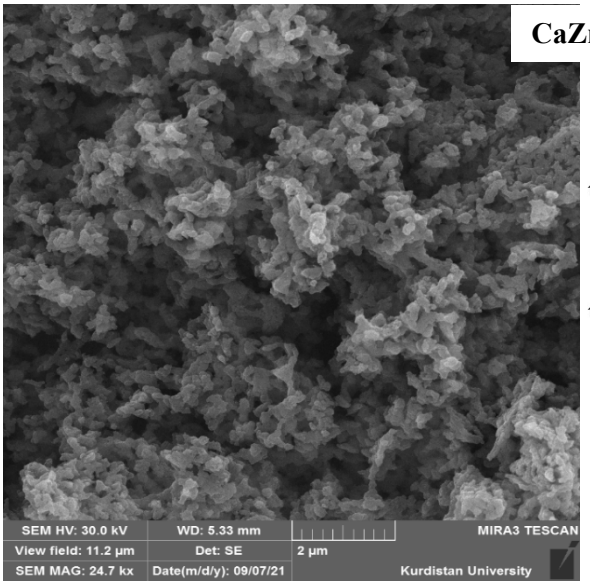

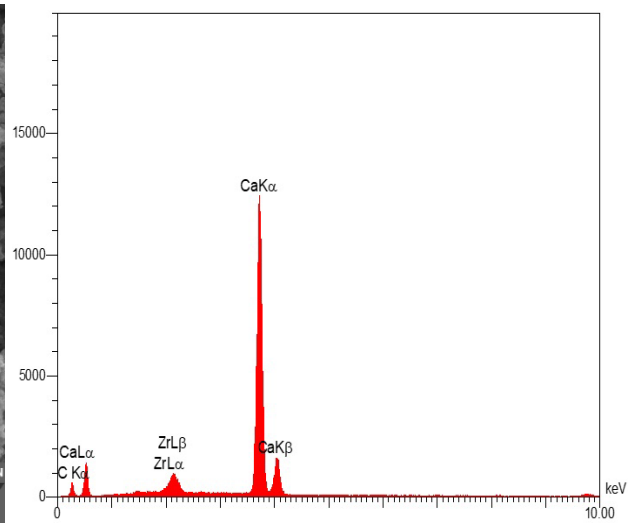

29

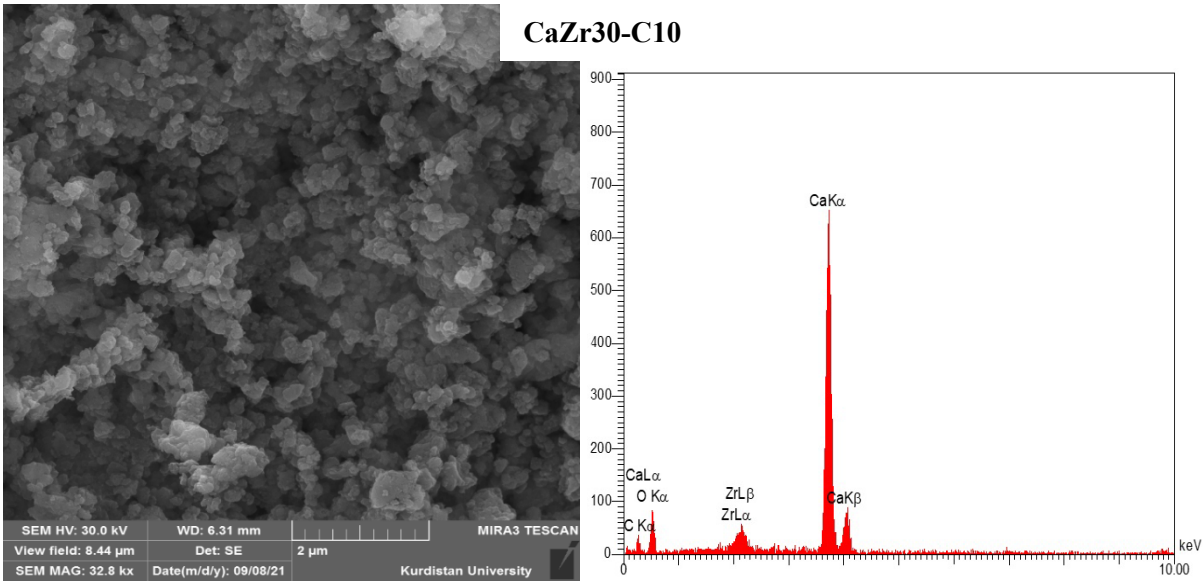

Fig. S2: SEM images and elemental EDS of pure CaO, CaZr15-C0, CaZr15-C2.5, CaZr15-C5, CaZr15-C10, CaZr30-C0, CaZr30-C2.5, CaZr30-C5, and CaZr30-C0.

CO_2 capture activity

To assess the role of CNT on the CO_2 uptake activity of CaZr15-C0 and CaZr, the CO_2 capture capacity of pure CaO, CaZr15-C0, CaZr15-C2.5, CaZr15-C5, and CaZr15-C10 during 1st and 15th cycles versus carbonation time is plotted in **Fig. S3a** and **b**, respectively. The highest initial capture capacity belongs to pure CaO due to its higher content of free CaO compared to Zr-promoted CaO sorbents containing 18.5 wt.% $CaZrO_3$. Since pure CaO suffers more from sintering and deactivation due to its lower thermal-durability feature and less porosity, the synthesized Zr-promoted sorbents present better CO_2 capture profiles than pure CaO at 15th cycles. The higher amount of CO_2 is adsorbed by CNT-templated samples compared to CaZr15-C0 at the 15th cycle. Even though CaZr15-C5 shows lower CO_2 capture capacity than CaZr15-C10 for an initial 5 min at the 15th cycle, ultimately, CaZr15-C5 adsorbs the more amount of CO_2 at the 15th carbonation step. However, over time, CaZr15-C5 presents a larger capture capacity than CaZr15-C10 at the ultimate cycle, indicating the more CO_2 capture capacity of CaZr15-C5 related to the capture process by CaO sites located in the interior zones. The larger volume of pore and porous zones in CaZr15-C5 than in

CaZr15-C10 results in a significantly more content of adsorbed CO_2 at the end of the carbonation stage.

It has been previously mentioned that merging CaO with costly ZrO_2 promoters decreases the available CaO for CO_2 capture during the formation of thermal-durable $CaZrO_3$. In this regard, the influence of CNT, in diverse contents of 2.5, 5, and 10 wt.%, on CaZr30-C0, containing the less $CaZrO_3$ content of 10 wt.% compared to CaZr15-C0 (18.5 wt.%), is assessed. **Fig. S3c** and **d** plot the CO_2 capture profiles of CaZr30-C0, CaZr30-C2.5, CaZr30-C5, and CaZr30-C10 during the carbonation time at the 1^{st} and 15^{th} cycles, respectively. The CNT-templated samples captured more CO_2 during the initial and final carbonation cycles compared to CNT-free counterparts, which similarly corroborates the effectiveness of CNT. Despite the identical CO_2 adsorption capacity at the swift carbonation step, the more porosity of CaZr30-C5 compared to CaZr30-C10 contributes to its better sorption activity in the slow carbonation stages, accompanied by the higher capture capacity of (0.372 g CO_2/g sorbent) than that of CaZr30-C10 (0.347 g CO_2/g sorbent) at 1^{st} cycles. Nonetheless, to a large extent, CaZr30-C5 and CaZr30-C10 exhibit equal capacity at the 15^{th} cycle (0.149 and 0.151 g CO_2/g sorbent).

Fig. S4a and **b** illustrate the CO_2 capture rate of pure CaO and prepared samples with a Ca/Zr molar ratio of 15/1 versus carbonation time at the 1^{st} and 15^{th} cycles. There are two distinct carbonation stages based on the CO_2 capture rate profile: a kinetically swift carbonation stage and a diffusion-controlled slow carbonation stage. The fast carbonation, which relates to the reaction of easy-accessible CaO surface with CO_2, consists of the uptrend CO_2 capture rate. Additionally, the slow carbonation stage corresponds to the reaction between CO_2 molecules and interior CaO sites in pores of sorbent texture. After reaching the maximum CO_2 capture rate, the fast carbonation stage terminates, and the slow carbonation stage starts with the diffusion of CO_2 into inner zones. Although prepared samples with a

Ca/Zr molar ratio of 15/1 demonstrate identical capture capacity at the fast carbonation stage, the more porous regions and pores' volume of CaZr15-C2.5, CaZr15-C5, and CaZr15-C10 cause the higher capture capacity at the diffusion carbonation stage. Due to the lower easy-accessible CaO surface, CaZr15-C0 reaches a higher maximum CO_2 capture rate at less time in 1st cycle, indicative of its less fast carbonation than CNT-templated counterparts. The main reason for the higher maximum CO_2 capture rate of CaZr15-C0 compared to CNT-templated samples is its higher free CaO content that utterly saturates at ~ 0.2 min. According to **Fig. S3b**, the higher uptake capacity of CaZr15-C10 rather than CaZr15-C5 for an initial 5 min of carbonation is associated with a significantly higher uptake rate at the termination of the quick carbonation stage, which can be attributed to its higher easy-accessible CaO cites. Comparing the CO_2 capture rate curves for 1st and 15 cycles demonstrates the effect of sintering on decreasing the fast carbonation time by ~ 50% owing to the sintering phenomenon and diminishing the easy-accessible CaO surface.

The CO_2 capture rate diagrams of samples developed with a Ca/Zr molar ratio of 30/1 at the 1st and 15th cycles, derived from **Fig. S3c** and **d**, are plotted in **Fig. S4c** and **d**. These figures indicate that the sintering rate of easy-accessible CaO sites over cycles reduces the fast carbonation span at the 15th cycle compared to the initial cycles. A higher CO_2 capture rate for CaZr30-C5 after ~1 and ~0.5 min at the 1st and 15th carbonation steps, respectively, can be ascribed to its more suitable textural and structural characteristics. Among developed samples with a Ca/Zr molar ratio of 30/1, the highest maximum CO_2 capture rates at the end of the 1st and 15th fast carbonation stages are reported in the case of CaZr30-C10.

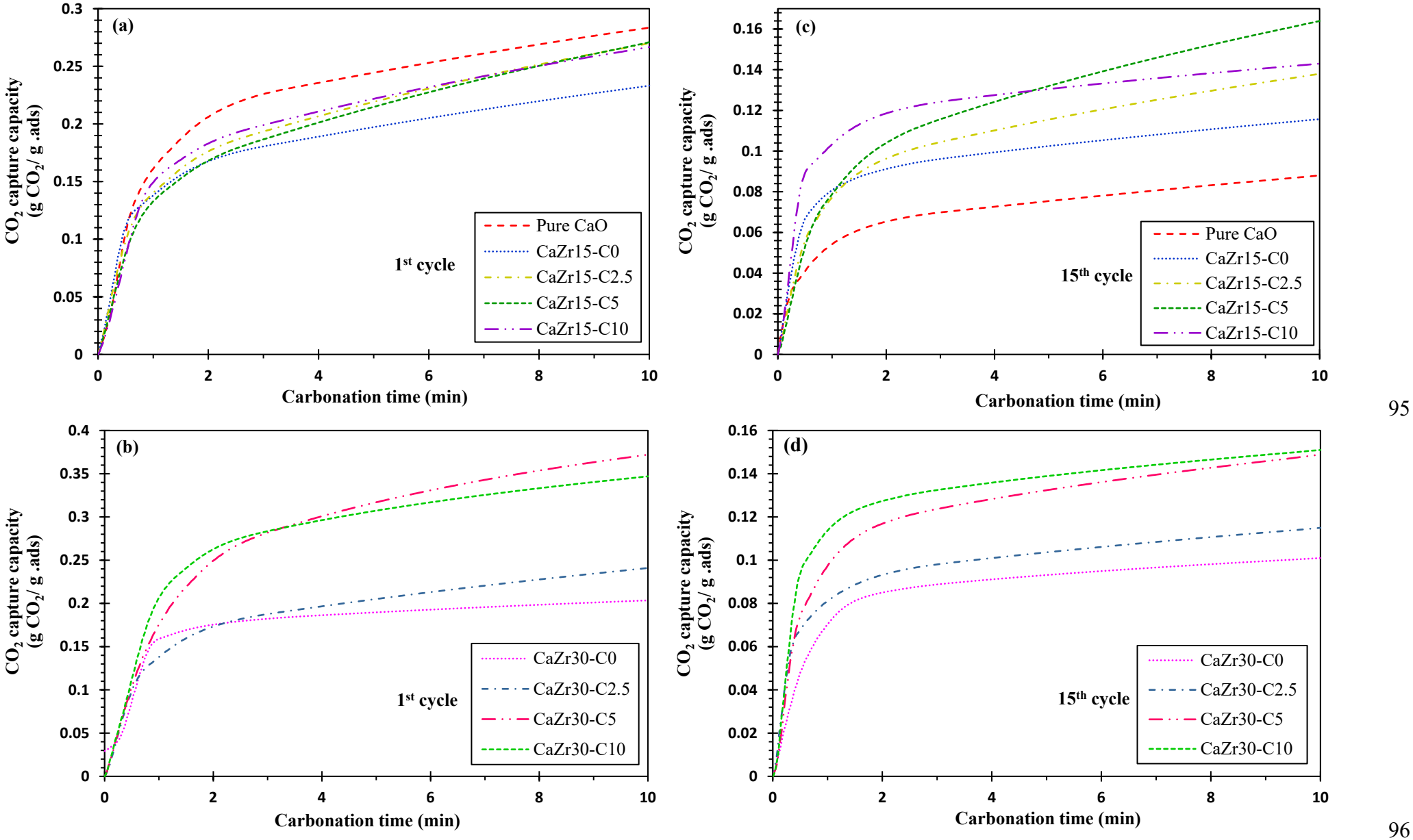

Fig. S3: Evaluation CO_2 capture capacity during carbonation time at 1st and 15th cycles for samples developed with Ca/Zr molar ratios of (a and b, respectively) 15/1 and (c and d, respectively) 30/1, under severe CaL conditions.

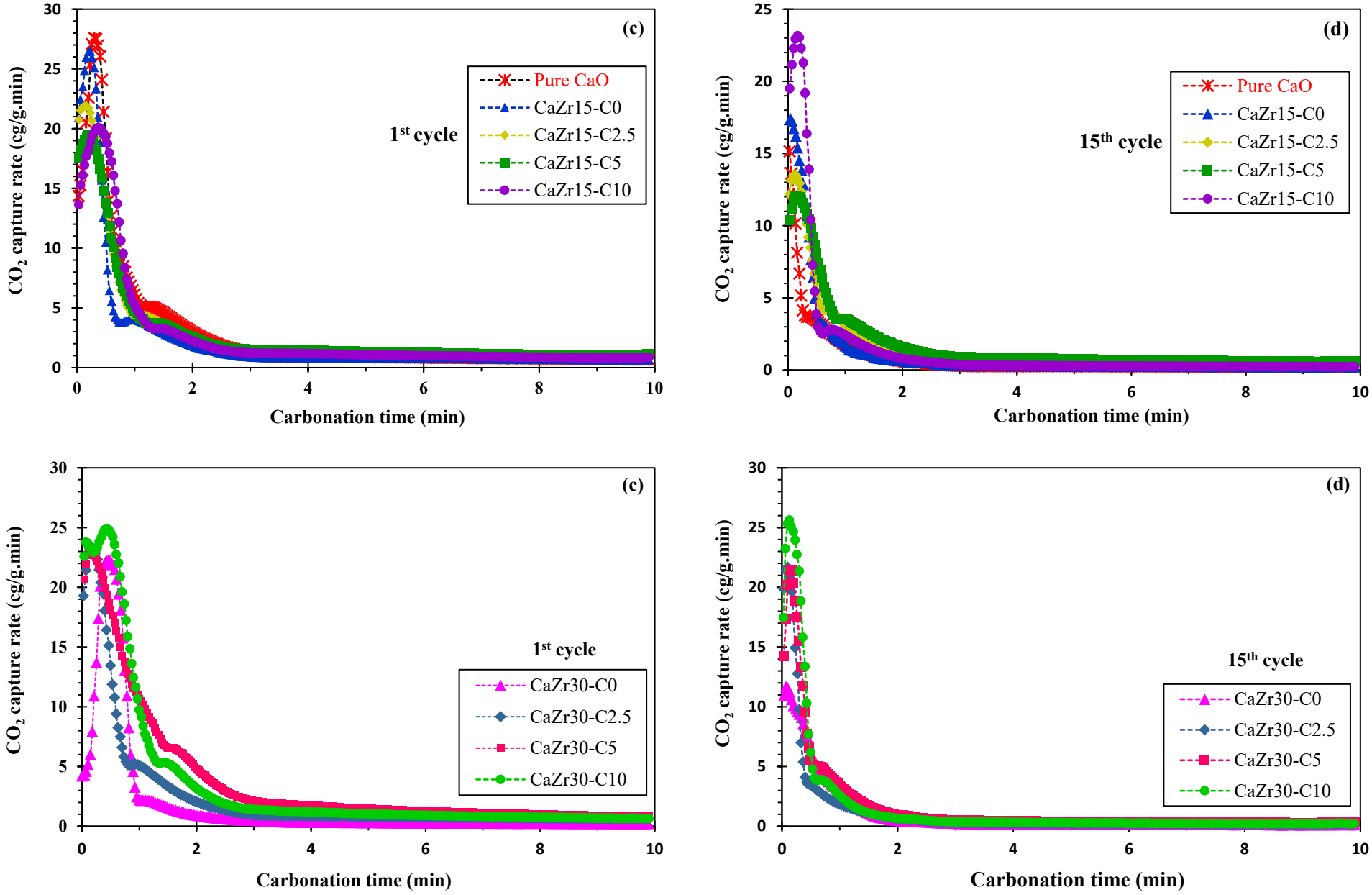

Fig. S4: Evaluation CO_2 capture capacity during carbonation time at 1st and 15th cycles for samples developed with Ca/Zr molar ratios of (a and b, respectively) 15/1 and (c and d, respectively) 30/1, under severe CaL conditions

The novel Carbon Nanotube-assisted development of highly porous CaZrO3-CaO xerogel with boosted sorption activity towards high-temperature cyclic CO2 capture

Heidari, Mohammad

2022-11-14

Heidari M, Mousavi SB, Rahmani F, et al., (2022) The novel Carbon Nanotube-assisted development of highly porous CaZrO3-CaO xerogel with boosted sorption activity towards high-temperature cyclic CO2 capture, Energy Conversion and Management, Volume 274, December 2022, Article number 116461

https://doi.org/10.1016/j.enconman.2022.116461